



HAL
open science

Infrared radiofluorescence (IR-RF) dating: A review

Madhav Krishna Murari, Sebastian Kreutzer, Georgina King, Marine Frouin, Sumiko Tsukamoto, Christoph Schmidt, Tobias Lauer, Nicole Klasen, Daniel Richter, Johannes Friedrich, et al.

► To cite this version:

Madhav Krishna Murari, Sebastian Kreutzer, Georgina King, Marine Frouin, Sumiko Tsukamoto, et al.. Infrared radiofluorescence (IR-RF) dating: A review. *Quaternary Geochronology*, 2021, 64, pp.101155. 10.1016/j.quageo.2021.101155 . hal-03170036

HAL Id: hal-03170036

<https://hal.science/hal-03170036>

Submitted on 22 Mar 2023

HAL is a multi-disciplinary open access archive for the deposit and dissemination of scientific research documents, whether they are published or not. The documents may come from teaching and research institutions in France or abroad, or from public or private research centers.

L'archive ouverte pluridisciplinaire **HAL**, est destinée au dépôt et à la diffusion de documents scientifiques de niveau recherche, publiés ou non, émanant des établissements d'enseignement et de recherche français ou étrangers, des laboratoires publics ou privés.

Copyright

1 **Infrared Radiofluorescence (IR-RF) dating: a review**

2 Madhav Krishna Murari^{1, 2}, Sebastian Kreutzer^{3, 4, *}, Georgina King⁵, Marine Frouin^{6, 7}, Sumiko
3 Tsukamoto⁸, Christoph Schmidt^{5, 9}, Tobias Lauer¹⁰, Nicole Klasen¹¹, Daniel Richter^{10, 12}, Johannes
4 Friedrich⁹, Norbert Mercier⁴, Markus Fuchs¹

5 ¹Department of Geography, Justus Liebig University, Giessen, Germany

6 ²Geochronology Project, Inter-University Accelerator Centre, New Delhi, India

7 ³Geography and Earth Sciences, Aberystwyth University, Aberystwyth, United Kingdom

8 ⁴IRAMAT-CRP2A, UMR 5060, CNRS - Université Bordeaux Montaigne, Pessac, France

9 ⁵Institute of Earth Surface Dynamics, Université de Lausanne, Lausanne, Switzerland

10 ⁶Department of Geosciences, Stony Brook University, Stony Brook, NY, United States

11 ⁷Research Laboratory for Archaeology and the History of Art, School of Archaeology, Oxford University,
12 Oxford, United Kingdom

13 ⁸Leibniz Institute for Applied Geophysics, Hannover, Germany

14 ⁹Chair of Geomorphology, University of Bayreuth, Bayreuth, Germany

15 ¹⁰Department of Human Evolution, Max Planck Institute for Evolutionary Anthropology, Leipzig,
16 Germany

17 ¹¹Institute of Geography, University of Cologne, Cologne, Germany

18 ¹²Freiberg Instruments GmbH, Freiberg, Germany

19 ***corresponding author:** sebastian.kreutzer@aber.ac.uk

20

21

22

23

24

25 **Abstract**

26 Luminescence dating methods on natural minerals such as quartz and feldspars are indispensable
27 for establishing chronologies in Quaternary Science. Commonly applied sediment dating
28 methods are optically stimulated luminescence (OSL) and infrared stimulated luminescence
29 (IRSL). In 1999, Trautmann et al. (1999a, b) proposed a new related technique called infrared
30 radiofluorescence (IR-RF). IR-RF denotes the infrared luminescence signal resulting from
31 exposure to ionizing radiation and potentially offers a significant methodological advance
32 compared to OSL and IRSL regarding luminescence signal stability, dating range and required
33 measurement time. The method has rarely been applied due to a lack of commercially available
34 measurement equipment but experienced a revival during the last years. The present article
35 provides a state-of-the-art overview of the physical background of IR-RF, its challenges,
36 applications and the potential as a dating method. The paper particularly addresses practical
37 considerations for applying IR-RF dating, including signal bleachability and saturation
38 behaviour, and summarizes proposed solutions.

39 **Keywords:** Infrared radiofluorescence; Radioluminescence; Feldspar; Chronology;
40 Luminescence dating

41 **1 Introduction**

42 In the late 1990s, Trautmann et al. (1998) characterized radioluminescence signals, the emission
43 stimulated by ionizing radiation, from various feldspar specimens to investigate their potential
44 for dating applications. Focusing first on radiation-induced emissions in the UV and yellow
45 wavelength range, where luminescence signal increases with radiation dose, they incidentally
46 observed the opposite for potassium bearing (K-) feldspar specimen such as microcline and
47 orthoclase: a dose-dependent signal decrease of the emission centred at 854 nm (1.45 eV; based
48 on peak tail fitting only). Later, Trautmann et al. (1999a, b), Schilles (2002) and Erfurt and
49 Krbetschek (2003a) determined that the emission peak was centred at 865 nm (1.43 eV).
50 Trautmann et al. (1998) recognized that this emission energy is similar to the excitation energy
51 used for infrared stimulated luminescence (IRSL, Hütt et al., 1988) and consequently interpreted
52 this process as a luminescent transition (trapping) of electrons. Their pioneer work paved the
53 way to what is known today as infrared radiofluorescence (IR-RF) dating; the method first
54 proposed by Trautmann et al. (1999a, b) and termed by Erfurt and Krbetschek (2003a, b).
55 The IR-RF signal is believed to be a direct measure of the fraction of empty electron traps, unlike
56 conventional luminescence dating methods such as those based on thermoluminescence (TL, cf.
57 Aitken, 1985a), optically stimulated luminescence (OSL, Huntley et al., 1985; Aitken, 1998) and
58 infrared stimulated luminescence (IRSL, Hütt et al., 1988), for which the signals are associated
59 with more complex recombination pathways. Since the IR-RF signal intensity *decreases* with
60 increasing dose, it can be used for dosimetry and dating purposes. IR-RF may provide
61 advantages over conventional single aliquot regenerative (SAR, Murray and Wintle, 2000) dose,
62 IRSL dating methods (e.g., SAR IRSL, Wallinga et al., 2000) or its derivatives deploying higher
63 reading temperatures (post-IR IRSL, Thomsen et al., 2008; MET-pIRIR, Li and Li, 2011a) in
64 terms of required measurement time (relatively short protocol, cf. Erfurt and Krbetschek, 2003b),
65 resolution of the dose-response curve (continuous recording of data points) and dating range
66 (Sec. 7). Nevertheless, IR-RF as a dating method is still subject to ongoing research, with its
67 general applicability being questioned (Buylaert et al., 2012). On the contrary, recent
68 technological and methodological work, e.g., on the optical resetting of the IR-RF signal, and
69 improved routines for dose estimation have yielded promising results (Frouin, 2014; Frouin et
70 al., 2015, 2017; Huot et al., 2015; Kreutzer et al., 2017; Murari et al., 2018).

71 This contribution provides an overview of past and recent developments of IR-RF from K-
72 feldspar as a dating method. We summarize current knowledge on existing models on the origin
73 of IR-RF, outline commonly applied measurement procedures and equipment, and highlight
74 shortfalls, challenges and open questions. Understanding what remains unknown may stimulate
75 discussions and lead to improved experimental designs towards a full establishment of IR-RF as
76 a valuable chronological tool.

77 **2 Origin of the IR-RF signal and relevant models**

78 The 1.43 eV (865 nm) IR-RF emission of K-feldspar (Trautmann et al., 1999a, b; 1.45 eV in
79 Trautmann et al., 1998, see below for an explanation) has the same energy as the typical
80 excitation maximum of IRSL (Hütt et al., 1988; Poolton et al. 2002a, b), which led Trautmann et
81 al. (1998) to suggest that both signals are derived from the same principal electron trap. More
82 recent observations of infrared photoluminescence (IR-PL; Prasad et al., 2017) seem to support
83 this hypothesis (see also Kumar et al., 2018). Further studies by Kumar et al. (2020) generally
84 confirmed this view but extended the understanding by assigning two different defect sites to the
85 principal trap based on their cathodoluminescence measurements.

86 Trautmann et al. (1999a, b) and Trautmann (2000) proposed a model for the IR-RF emission of
87 feldspar whereby IR-RF results from the transition of an electron from the conduction band to
88 the ground state of the IRSL trap through the excited state.

89 Figure 1 illustrates the different electronic transitions associated with IRSL and IR-RF
90 production in one plot. Please note: Although we compiled different ideas in one figure, our
91 graphical representation *should not* be considered a new model. In Fig. 1, continuous exposure to
92 ionizing radiation leads to a constant flow of electrons from the valence band to the conduction
93 band [a], from which electrons can either recombine radiatively [b] or non-radiatively (not
94 shown for clarity), or become trapped [c]. As irradiation persists, the IRSL trap [c] becomes
95 filled, resulting in more electrons recombining radiatively [b], accounting for the observed rise in
96 the ultraviolet (UV)-RF and visible light (VIS)-RF emissions at higher doses (Trautmann et al.,
97 1999a). However, this model raises two major questions: (1) why does the IR-RF signal not fully
98 saturate during laboratory irradiation, resulting in a zero or negligible IR-RF signal, and (2) to
99 bleach, why does the IR-RF signal require exposure to light of higher energies than IR (e.g.,

100 Trautmann et al., 1998, 1999a, b; Frouin et al., 2015, 2017), whereas the IRSL signal from the
101 same trap could be efficiently reset through exposure to infrared light?

102 ***Figure 1***

103 ***(Models)***

104 To explain why the IR-RF signal does not appear to saturate, Trautmann et al. (1999a) first
105 considered electron release throughout irradiation due to the low thermal stability of the IRSL
106 trap, resulting in the replenishment of free electron-hole pairs and thus a continuously decaying
107 IR-RF signal. However, this hypothesis contradicts a measured lifetime of the IRSL trap in the
108 range of Ga (Murray et al., 2009). An alternative explanation not considered by Trautmann et al.
109 (1999a) is the loss of trapped electrons by athermal tunnelling, known as anomalous fading of
110 feldspar (e.g., Wintle 1973; Spooner 1992; Visocekas, 1993; Huntley and Lian, 2006) and more
111 specifically, the anomalous fading of the IRSL feldspar trap (e.g., Spooner 1992; Huntley and
112 Lamothe, 2001) (transition [d] in Fig. 1), which we summarised in Sec. 5.6. Instead, Trautmann
113 et al. (1999a) preferred a model already suggested by Schön et al. (1942) and Klasens (1946) for
114 sulphide phosphors, with a proposed transfer of holes from the valence band to the IRSL trap
115 throughout irradiation, effectively increasing the defects trapping capacity (transition [e] in Fig.
116 1).

117 To address the different bleaching behaviour of IR-RF and IRSL signals,
118 Trautmann et al. (2000a) modified their earlier model, relating the bleaching of the IRSL signal
119 to localized electron transitions after the suggestion by Poolton et al. (1995). Following IR
120 exposure, an electron is only excited to the excited state of the trap ([f] in Fig. 1), which is paired
121 with the excited state of a neighbouring recombination centre, allowing a localized transition.
122 Thus, the IRSL emission would relate to the radiative relaxation of the electron to the ground
123 state of the recombination centre. Trautmann (2000) and Trautmann et al. (2000a) determined
124 from pulse-annealing experiments that bleaching of the IRSL trap is limited by the number of
125 available recombination centres, suggesting thermal instability of trapped electrons could reduce
126 the density of holes. They drew this conclusion from the IR-RF signal's stability up to
127 temperatures of 400 °C, whereas IRSL and the related VIS-RF signals depleted at temperatures
128 >300 °C. Trautmann (2000) and Trautmann et al. (2000a) concluded that the IRSL electron-hole

129 population accounts for only ~1.5 % of the total potential IRSL trap occupancy, implying that
130 most of these trapped electrons do not have the possibility of recombining with a hole during IR
131 stimulation. A phenomenon that Trautmann (2000) and Trautmann et al. (2000a) did not
132 consider, and which may influence these effects to some extent, is athermal signal loss (i.e.,
133 anomalous fading). Following the model of Huntley (2006), ground state tunnelling [d in Fig. 1]
134 would result in preferential recombination of unstable charge with proximal recombination
135 centres, which may otherwise have been involved in localized transitions from the IRSL trap.
136 Athermal de-trapping results in a non-linear increase of IRSL with dose, an effect recorded and
137 highlighted by Trautmann (2000) and Trautmann et al. (2000a).

138 **2.1 Defects related to IR-RF and IRSL**

139 The exact identification of defects responsible for electron and hole trapping in feldspar is
140 subject to ongoing research, and as such, the physical nature of the IRSL and IR-RF trap remains
141 under debate. The traps and recombination centres of K-feldspars have mainly been assigned
142 based on indirect measurements and correlation studies (e.g., Baril and Huntley, 2003a; Erfurt
143 2003a, b; Erfurt and Krbetschek, 2003b). Krbetschek et al. (1997) discussed the principal K-
144 feldspar luminescence emissions and their possible origins for different excitation methods. The
145 most common emission bands for K-feldspar are listed in Table 1 (please also note the references
146 given therein).

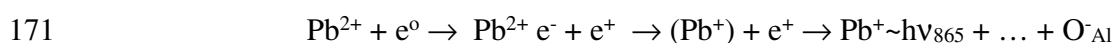
147 *Table 1*

148 *(Traps and recombination centres)*

149 It appears that in the literature Fe^{3+} and Pb^+ ions have been identified as the main centres which
150 are believed to be responsible for the presence of the red to deep-red emission (~ 1.7 eV; Prasad
151 and Jain, 2018) in feldspar. Kumar et al. (2018) tried to correlate their IR-PL findings (Prasad et
152 al., 2017) with the IR-RF signal. Their work suggested that the same defect participated in the
153 production of IR-RF and IR-PL. However, they speculated that IR-PL, contrary to IR-RF, is
154 “site-selective”, i.e. IR-PL preferentially probes centres leading to the emission at ca 1.30 eV
155 (955 nm) whereas the IR-RF emission may be ‘contaminated’ by emissions from other centres,
156 such as Fe^{3+} , related to the emission band near 680 nm to 740 nm (e.g., Geake et al., 1977; Telfer
157 and Walker, 1975; White et al., 1986; Brooks et al., 2002; Finch and Klein, 1999; Krbetschek et

158 al., 2002; Prasad and Jain, 2018). Most recent work by Kumar et al. (2020), reporting infrared
159 cathodoluminescence (IRCL) experiments at 7 K, give evidence for a correlation of emission
160 peak position and K-concentration. They further propose Fe⁴⁺ as a defect competing for electrons
161 with the principal trap. Furthermore, the red emission's peak location has been observed to be
162 related to the composition of feldspar samples (e.g., Finch and Klein, 1999; Krbetschek et al.,
163 2002). In contrast, the Pb⁺ centre appears to be related to the IR-RF emission bands between ca.
164 860 nm and 910 nm (e.g., Nagli and Dyachenko, 1988; Erfurt 2003a, b; Erfurt and Krbetschek,
165 2003a).

166 Erfurt (2003a) and Erfurt and Krbetschek (2003a) observed an increase of IR-RF signal intensity
167 with increasing Pb content for concentrations on the order of 30 ppm to 1,400 ppm, and proposed
168 that the IR-RF emission may be associated with the excitation of Pb²⁺ to monovalent (Pb⁺)*
169 which subsequently relaxes to the ground state of Pb⁺, emitting photons at 1.43 eV.
170 Schematically it reads (adapted from Ostrooumov 2016, p. 152 for amazonite):



172 However, this hypothesis remains unproven, and earlier electron paramagnetic resonance (EPR)
173 studies have indicated that Pb⁺ is only found in amazonite, a specific type of microcline where
174 Pb⁺ occupies a K⁺ position (Marfunin and Bershov, 1970; Marfunin, 1979). In contrast, Poolton
175 et al. (2002b) hypothesised that the IRSL trap is a simple hydrogenic defect, calculating an
176 optical transition at 1.48 ± 0.04 eV, close to that observed in the K-Na feldspar series.

177 **2.2 IR-RF model and related phenomena**

178 Since Trautmann et al. (1998, 1999a, 2000a) proposed a model to explain the processes of (IR)-
179 RF of feldspar, our understanding of luminescence processes in feldspar has improved
180 considerably, driven mainly by the developments around conventional IRSL (e.g., Wallinga et
181 al., 2000; Huntley and Lamothe, 2001; Lamothe et al., 2003; Auclair et al., 2003; Murray et al.,
182 2009; Kars and Wallinga 2009; Pagonis and Kulp, 2017; Pagonis et al., 2013, 2019; Lamothe et
183 al., 2020), the post-IR IRSL (also pIRIR) measurement protocols (Thomsen et al., 2008; Buylaert
184 et al., 2009), time-resolved IRSL investigations (e.g., Jain and Ankjærsgaard, 2011) as well as IR-
185 PL (Prasad, 2017; Prasad et al., 2017, 2018; Kumar et al., 2020).

186 Figure 1 shows a band-gap diagram which describes models for IRSL, post-IR IRSL and IR-RF.
187 The presence and importance of the sub-conduction band tail-states are now widely recognized
188 (Poolton et al., 2002a, 2009; Jain and Ankjærgaard, 2011) and anomalous fading (athermal
189 signal loss; Wintle, 1973 for TL; Spooner 1992 for stimulation at 514.5 nm and ~880 nm) from
190 the IRSL trap is generally regarded as ubiquitous in feldspar (e.g., Huntley and Lamothe, 2001)
191 (transition [d] in Fig. 1). The largest inconsistency between the IR-RF models and more recent
192 studies is that the former models did not consider the effects of hole distribution (i.e.,
193 recombination distance) and anomalous fading.

194 Excitation spectra of feldspar revealed the characteristic resonance at ~1.4 eV (1.43 eV, Hütt et
195 al., 1988; see also above), which is superimposed on a rising continuum, now recognized as
196 relating to the sub-conduction band-tail states (Poolton et al., 2002a, 2009). IRSL preferentially
197 samples electrons which can recombine with proximal holes, either through tunnelling from the
198 ground state of the IRSL trap (transition [d] in Fig. 1) or via a localized transition (transition [f]
199 in Fig. 1). Higher energy stimulation of the IRSL trap or higher temperature stimulation
200 (phonon-assisted diffusion) allows electrons to recombine via diffusion through the band-tail
201 states (Poolton et al. 2002a; Jain and Ankjærgaard, 2011) (transition [g] in Fig. 1). For post-IR
202 IRSL signals, which are measured at elevated temperatures of typically 225 °C or 290 °C
203 (pIRIR₂₂₅ or pIRIR₂₉₀), this enables more distal recombination centres to be accessed (Jain and
204 Ankjærgaard, 2011), which have greater athermal (Huntley 2006; Jain and Ankjærgaard, 2011)
205 and thermal stability (Thomsen et al., 2010; Li and Li, 2011b, 2013; Fu et al., 2012). However,
206 pIRIR signals are systematically harder to bleach than IRSL signals (e.g., Li and Li, 2011a).

207 In general, the IR-RF signal is known to bleach less efficiently than the low-temperature IRSL
208 signal with infra-red light (Trautmann, 1999; Trautmann et al., 1999a; Frouin, 2014; Frouin et
209 al., 2015) and recently it has been shown that the bleaching rate is similar to that observed for the
210 pIRIR₂₉₀ signal (Frouin et al., 2017). This comparably slow bleachability agrees with the
211 apparently high thermal stability of the IR-RF signal (at least up to 350 °C, cf. preheat vs curve
212 shape experiments by Erfurt and Krbetschek, 2003b, their Fig. 7). However, further
213 investigations are required to constrain the thermal stability of IR-RF signal and its susceptibility
214 to anomalous fading.

215 **3 Measurement devices**

216 The first IR-RF studies were carried out on home-made systems (Trautmann et al., 1998, 1999a;
217 Schilles and Habermann, 2000; Erfurt et al., 2003), which differ from the ready-to-use systems
218 available today (Lapp et al., 2012; Richter et al., 2013). The device described in Trautmann et al.
219 (1998) was equipped with a spectrometer for K-feldspar IR-RF exploration. However, because
220 the spectrometer was limited to 800 nm (Trautmann et al., 1998, 1999b), first peak investigations
221 were based on signal extrapolation (Trautmann et al., 1998). After identifying the dose-
222 dependent peak (Trautmann et al., 1999a) at 865 nm, the integrated RF signal around this peak
223 was used for RF dose estimation. Schilles and Habermann (2000) and Erfurt (2003b) went one
224 step further and attached a photomultiplier tube with a filter combination optimized to limit the
225 measured luminescence to the 865 nm emission closely. Tables 3 and 4 summarize the details of
226 various instruments concerning signal detection and sample bleaching parameters. Figures 2 A–
227 D provide different technical realizations for measuring the RF signal from K-feldspar samples.

228 *Figure 2 A B C D*

229 *(All IR-RF devices)*

230 **3.1 Stimulation or irradiation unit**

231 Radiofluorescence (RF) is the light emission caused by ionizing radiation. Therefore, stimulation
232 sources can either be ionizing charged particles (ions, electrons or protons) or high energy
233 photons (X-ray or γ -ray). The custom-made devices were equipped with $^{137}\text{Cs}/^{137}\text{Ba}$ sources ($t_{1/2}$
234 ~ 30.08 a) (Schilles and Habermann, 2000), while other (commercially) available RF equipment
235 has $^{90}\text{Sr}/^{90}\text{Y}$ sources ($t_{1/2} \sim 28.8$ a) (Lapp et al., 2012; Richter et al., 2012, 2013). Details of the
236 radiation sources are provided in Table 2. The major differences between these radiation sources
237 are activity, radiation type and energy spectra. The $^{137}\text{Cs}/^{137}\text{Ba}$ radiation sources in the home-
238 made devices, e.g., used by Trautmann et al. (1999a), Schilles (2002) and Erfurt et al. (2003),
239 emit β -particles and γ -photons with mean energies of 187.1 keV and 662 keV, respectively. At
240 the same time, ^{137}Cs is also a γ -photon emitter, but the IR-RF stimulation by γ -rays was
241 considered being negligible in comparison to the β -particles (Trautmann, 1999, p. 16). The
242 $^{90}\text{Sr}/^{90}\text{Y}$ source emits a broad energy spectrum with mean β -energies around 195.8 keV. Other

243 differences regarding the stimulation sources are the design and the way of irradiating the sample
244 (planar radiation source geometry vs ring source geometry). The ring source design (Richter et
245 al., 2012) allows the detector to be mounted directly above the source. For the planar sources, the
246 light collection is realized by an optical light guide (Lapp et al., 2012) or using light reflected to
247 the detector (Schilles, 2002). The indirect light collection has the advantage of reducing
248 unwanted signal contributions induced in the detection system due to bremsstrahlung, but it
249 usually comes at the cost of reduced detection efficiency. Additionally, the ring-type sources
250 have been reported as delivering a highly spatially homogenous dose rate (Richter et al., 2012),
251 relative to planar sources. Common to all types of sources and geometries is the underlying
252 assumption of measuring a comparable IR-RF signal.

253 *Table 2*

254 *(Irradiation units)*

255 **3.2 Detection and filter combination**

256 Initial studies on IR-RF were based on spectrometer measurements to identify IR-RF peaks and
257 characterize their behaviour. Trautmann et al. (1998) identified the presence and behaviour of the
258 IR-RF peak around 854 nm based on curve fitting of a partially measured peak, but later
259 (Trautmann et al., 1999a, b) reassigned the peak position to 865 nm using an improved
260 spectrometer. Erfurt (2003b) and Schilles (2002) studied this peak in detail with a spectrometer
261 and a photomultiplier tube in conjunction with optical filters (Sec. 5.1). The spectrometers'
262 relevant details are provided in Table 3, and Fig. 3 shows the efficiency of different spectrometer
263 systems.

264 *Table 3*

265 *(Spectrometer overview)*

266 *Figure 3*

267 *(Spectrometer transmission)*

268 Table 4 provides detailed detector settings applied to measure the IR-RF signal. The main
269 difference between the devices is the filter combination, and thus the detection window.
270 However, all types of filters centre around 865 nm and the usage of different filters reflects

271 mainly the availability of filters when the equipment was delivered. Trautmann et al. (1999a)
272 recommended centring around 865 nm and avoiding interference from the 710 nm peak. This
273 idea was also followed by Erfurt and Krbetschek (2003b) using a detection window of 865 ± 20
274 nm, considering the broadening effect of the 710 nm peak with increasing dose (Sec. 5.1). The
275 devices used by Schilles (2002) and Erfurt (2003b) both had the same type of photomultiplier
276 tube (PMT) (Hamamatsu R943-02) with a quantum efficiency of ~5 % at 865 nm. The quantum
277 efficiency of commercial *lexsyg* and *Risø* readers is about ~12 % at that wavelength, both
278 employing the same PMT (Hamamatsu H7421-50), but the efficiency drops to 0.001 % for
279 wavelengths > 900 nm. The PMTs of these commercial devices have a lower efficiency for the
280 potentially interfering signals > 900 nm but relatively high efficiency for the 710 nm peak (Erfurt
281 and Krbetschek, 2003b), which might significantly interfere with the main IR-RF peak. The
282 bandpass for different systems used in the past and present are shown in Figs. 4 A and B.

283 **Table 4**

284 *(detector settings)*

285 **Figure 4 A B**

286 *(PMT efficiency and filter combinations)*

287 **3.3 Bleaching units**

288 Table 5 summarizes the information on the commonly used bleaching units. In the device used
289 by past researchers (e.g., Schilles and Habermann, 2000; Erfurt et al., 2003) the sample geometry
290 was fixed, i.e., the sample was not moved between different measurement steps. Thus, the IR-RF
291 signal's bleaching was done by connecting a solar lamp using an optical fibre. In this design, IR
292 cut-off filters were used to avoid excess heating due to the high intensity of light of the solar
293 lamp. In contrast, inside commercial devices for IR-RF measurement and bleaching (e.g., *lexsyg*
294 and *Risø*) the sample moves to different positions. The *Risø* system is equipped with powerful
295 UV LEDs (~700 mW), and the *lexsyg* device has an inbuilt LED solar simulator that combines
296 up to six wavelengths with the option of varying the power of each LED (Richter et al., 2013; see
297 Table 5).

298 **Table 5**

299

(bleaching units)

300 **3.4 Sample geometry**

301 Krbetschek et al. (2000) and Erfurt and Krbetschek (2003b) recommended a fixed geometry
302 during IR-RF measurements. They observed a high dispersion in IR-RF dose distributions
303 attributed to geometry changes (e.g., grain movements) when samples were bleached outside the
304 reader. Buylaert et al. (2012) did not observe any changes in the IR-RF signal due to the
305 movement of the sample from one position to another (cf. Fig 3b in Buylaert et al., 2012).
306 Similarly, Frouin et al. (2015, 2017) did not report dose dispersions caused by the movement of
307 the sample inside the reader for their measurements using a *lexsyg research* reader. Later,
308 Kreutzer et al. (2017) attributed a large part of the inter-aliquot scatter to unwanted machine-
309 induced geometry changes, which, however, may have affected only their particular reader.
310 Nevertheless, in summary, it appears to be advisable to aim for a stable sample geometry and
311 check the results for unwanted effects, enlarging the D_e distribution (cf. Kreutzer et al., 2017).

312 **4 Sample preparation methods**

313 IR-RF sample preparation methods extract K-feldspar enriched mineral grains following routine
314 procedures (e.g., Preusser et al., 2008). After sieving and chemical treatments with HCl and
315 H₂O₂, density separation using heavy-liquids (e.g., lithium heteropolytungstates or sodium
316 polytungstate) extract feldspar grains. Additional (froth) flotation (e.g., Herber 1969; application
317 examples: Miallier et al., 1983; Sulaymonova et al., 2018) can be applied to enrich the K-
318 feldspar concentration further; a procedure that the Freiberg group has mainly used in the context
319 of IR-RF (e.g., Trautmann, 1999; Erfurt 2003b). Flotation likely provides a better yield in terms
320 of better separation of quartz and feldspar mineral phases. Despite requiring extra laboratory
321 equipment and staff training, flotation has unmined potential for further enriching the K-feldspar
322 fraction (e.g., via selective flotation: Larsen et al., 2019) with possible implications for measured
323 IR-RF signals.

324 To remove the outer α -irradiation affected layer of coarse K-feldspar grains ($> 90 \mu\text{m}$) a low
325 concentration ($\leq 10 \%$) HF treatment was often used (e.g., Wagner et al., 2010; Lauer et al.,
326 2011). However, the practice of etching of coarse grain K-feldspar was already questioned by

327 Duller (1992), who described non-uniform etching along the lines of weakness within the
328 mineral. Porat et al. (2015) recalled caution if HF is applied to feldspar grains because HF
329 etching might significantly modify the luminescence properties of K-feldspar, and thus Porat et
330 al. (2015) suggest etching times <15 min. Frouin et al. (2017) reported inconclusive, younger and
331 highly scattered, IR-RF results for two samples (BT714, BT715) after prolonged HF treatment
332 (10 %, 40 min), while this was not observed for another, non-etched, sample from the same site
333 (BT706). Although the systematic effect of HF treatments with different timings and
334 concentration on the IR-RF signal remains unexplored, HF treatment appears to be dispensable.

335 **5 IR-RF signal characteristics**

336 **5.1 IR-RF spectroscopy: Signal identification and measurement optimization**

337 The IR-RF signal composition was extensively studied using a home-made spectrometer in
338 combination with a liquid nitrogen-cooled charged coupled device (CCD) detector (Trautmann et
339 al., 1998, 2000b; Krbetschek and Trautmann, 2000). Their spectroscopic investigations of IR-RF
340 from feldspar revealed many peaks centred at various wavelengths. However, the 865 nm
341 emission peak was found to be stable with its intensity decreasing with increasing dose. K-
342 feldspar showed the highest signal intensity at this wavelength compared to other feldspar
343 compositions. Trautmann (1999) and Schilles (2002) noticed that the spectrum of K-feldspar
344 could be fitted with two Gaussian functions centred at 710 nm (1.75 eV) and 865 nm (1.43 eV).
345 Later, Erfurt (2003b) improved the spectrometer used by Trautmann (1999) and recognized that
346 the data required a minimum of three Gaussian functions to fit the emission spectrum, with a
347 third emission centred at ~910 nm (1.35 eV; Erfurt and Krbetschek, 2003a). The spectroscopic
348 study of these peaks provided the appropriate detection range (filter combination) required for
349 isolating the main IR-RF peak at 865 nm from other neighbouring emissions (Krbetschek et al.,
350 2000). A typical raw spectrum for K-feldspar shows many emission peaks (Fig. 5C after
351 Schilles, 2002) and Trautmann et al. (1999a) demonstrated that the peak intensity at 865 nm
352 decreases with increasing dose, whereas the intensity of the 710 nm peak increases with dose.
353 Furthermore, Trautmann et al. (1998) observed that the 710 nm peak is unstable and vanished
354 within a few hours following irradiation.

355 Both the 710 nm and 910 nm¹ emissions may interfere with the main IR-RF peak (865 nm),
356 which filters can minimise. The effect of such a filter can be simulated using three superimposed
357 Gaussian functions (Fig. 5A and Fig. 5B similar to Erfurt and Krbetschek, 2003b). Table 4
358 summarizes all devices' filter combinations to isolate the peak centred at a wavelength of 865
359 nm.

360 *Figure 5 A B C*

361 *(IR-RF peaks in feldspar)*

362 **5.2 IR-RF signal resetting**

363 The success of (optical) luminescence dating methods relies on resetting the luminescence signal
364 during sediment transport prior to burial. For IR-RF, the signal intensity increases with light
365 exposure after several minutes to several hours and reaches its highest value when all traps are
366 empty. The bleachability of the IR-RF signal was assessed by bleaching until a plateau is formed
367 between the IR-RF signal vs bleaching time. A constant plateau indicates no further signal
368 increase, i.e., the IR-RF signal is at its maximum, and all IR-RF related traps are empty. In the
369 first IR-RF bleaching experiments (Trautmann et al., 1999a), natural direct sunlight (VIS to UV
370 component, Fig. 6A) was used for a few hours (between 2 h and 5 h of daylight exposure in
371 February in Freiberg, Germany) to bleach the IR-RF signal. Later, Trautmann et al. (2000a)
372 showed that wavelengths shorter than 500 nm were more efficient at resetting the IR-RF signal
373 (Fig. 6B) and Krbetschek et al. (2000) demonstrated that only a few minutes (~5–10 min) were
374 required to reset the signal, using a 200 W Hg-lamp (Table 5 for an overview of the settings)
375 along with a heat-absorbing filter (Fig. 6C). Further bleaching experiments were conducted using
376 a 300 W OSRAM 'Ultravitalux' sunlamp placed at a distance of 35 cm from the aliquot for 6.5 h
377 (Krbetschek et al., 2000) or an on-board lamp (250 W OSRAM metal halide), using fibre optics,
378 which delivered ~100 mW cm⁻² to the aliquot for 30 min.

379 *Figure 6 A B C D*

380 *(Bleaching)*

¹920 nm in Erfurt and Krbetschek (2003b), however, henceforth termed '910 nm' emission.

381 Buylaert et al. (2012) compared the D_e values of samples with independent age control. They
382 obtained different values between aliquots that were bleached with UV LEDs (delivering 700
383 mW cm^{-2}) with an exposure time of 25 min, compared to bleaching with a Hönle SOL 2 solar
384 simulator for 4 h. Samples bleached with the Hönle SOL2 resulted in older, but partly also more
385 consistent ages compared to the independent age control (cf. Buylaert et al., 2012, their Fig. 7).
386 Later Varma et al. (2013) concluded that exposure of 800 s is optimal for resetting the IR-RF
387 signal using the aforementioned UV LED (delivering 700 mW cm^{-2}).

388 Frouin et al. (2015) systematically compared the bleaching behaviour of monochromatic light
389 and a solar simulator spectrum. In their study, they showed that: i) K-feldspars of various origins
390 exhibit the same behaviour during bleaching experiments, and ii) the IR-RF signal can be
391 bleached by all wavelengths, ranging from 365 nm to 850 nm, and iii) the IR-RF signal can be
392 completely reset in nature and cannot be “over-bleached” in the laboratory even with the use of
393 longer time exposures. Finally, they recommend a solar spectrum close to the terrestrial solar
394 spectrum with minimal UV light contribution. They achieved this by individually adjusting the
395 monochromatic LEDs' power in their luminescence reader and stated that this spectrum delivered
396 a sufficient amount of power (375 mW cm^{-2}) to bleach the IR-RF signal in minimum time at
397 ambient temperature (Frouin et al., 2015). Furthermore, they showed that the onset of a
398 bleaching plateau started after 3 h to 4 h of light exposure (cf. Fig. 4 in Frouin et al., 2015).
399 Specifically, within this light spectrum, the power of the UV (325 nm) LED was reduced to 10
400 mW cm^{-2} as this wavelength is absorbed by the atmosphere and its presence in the terrestrial
401 solar spectrum is minimal. Regardless, this low power, Frouin (2014, her Fig. 28) showed that
402 UV bleaches most efficiently within the first seconds before it reaches a plateau after ca. 40 h.
403 Although an artificial bleaching spectrum using only six wavelengths (LEDs) cannot match the
404 terrestrial solar spectrum, it may remain a good approximation of natural bleaching conditions
405 (typical irradiance on Earth of 90–100 mW cm^{-2} ; ASTM international, 2012). A comparison
406 between the bleaching behaviour of the IR-RF signal measured at 70 °C (Sec. 6.1) with other
407 variants of the IRSL signals of K-feldspar showed that IR-RF seems to bleach at a similar rate to
408 the pIRIR_{290} signal but much slower than the IRSL_{50} signal (Frouin et al., 2017; Fig. 6D).
409 However, a similar bleaching rate compared to the pIRIR_{290} signal does not guarantee a complete
410 reset of either signal (i.e., pIRIR_{290} and IR-RF); various studies have shown that the pIRIR_{290}

411 signal is hard to bleach and can have large residual doses even after 4 h of solar simulator
412 bleaching (e.g., Buylaert et al., 2012; Li et al., 2014). It may take up to ~300 h to reach a
413 constant residual dose (Yi et al., 2016). In summary, Frouin et al. (2015) recommended a
414 minimum of 3 h bleaching using the inbuilt solar simulator of their equipment with the following
415 settings: 365 nm (10 mW cm⁻²), 462 nm (63 mW cm⁻²), 525 nm (54 mW cm⁻²), 590 nm (37 mW
416 cm⁻²), 623 nm (115 mW cm⁻²), and 850 nm (96 mW cm⁻²).

417 **5.3 Phosphorescence**

418 In the context of IR-RF, two types of phosphorescence have been observed: (1) Phosphorescence
419 after bleaching (Fig. 7) and (2) phosphorescence after irradiation (so-called
420 radiophosphorescence). *Phosphorescence after bleaching* was considered by Erfurt and
421 Krbetschek (2003b). They recognized that K-feldspar samples, bleached with a solar simulator,
422 show a very strong phosphorescence at 865 nm. For a sediment sample with a palaeodose of
423 ~1,500 Gy, extrapolation of the phosphorescence signal at room temperature using an
424 exponential decay shows that its effect lasts beyond 1,000 s after bleaching (cf. Fig. 6 in Erfurt
425 and Krbetschek, 2003b). To accommodate this effect in IR-RF measurement protocols, Erfurt
426 and Krbetschek (2003b) recommended a pause of one hour after bleaching, before starting the
427 next IR-RF measurement. In contrast, Buylaert et al. (2012) showed that after bleaching the
428 phosphorescence signal intensity is lower by two orders of magnitude than IR-RF, its effect on
429 the main IR-RF signal will be negligible. However, it should be noted that their setup differs
430 from the one used by Erfurt and Krbetschek (2003b) (Sec. 3). Varma et al. (2013) reported that
431 although the IR-RF signal of their sample was almost at its saturation level, it did not show
432 significant phosphorescence after bleaching the sample for 800 s. Hence, they concluded that no
433 extra pause is needed and suggested that a delay of 500 s is sufficient to reduce the
434 phosphorescence down to the background level if the bleaching time is less than 800 s. Similarly,
435 Schaarschmidt et al. (2019) reported a weak phosphorescence compared to the IR-RF signal and
436 reduced the pause to 900 s for their samples. In summary, it seems that phosphorescence caused
437 by bleaching can be avoided by introducing a pause of 15 min to 1 h prior to IR-RF
438 measurements (Erfurt and Krbetschek, 2003b; Frouin et al., 2015; Schaarschmidt et al., 2019) in
439 the case of solar simulator bleaching and may not be required if the sample is bleached with a
440 UV LED for 800 s or longer (Varma et al., 2013).

441 *Radiophosphorescence* is a known phenomenon used in the past to characterize luminescence
442 spectra from feldspar (e.g., Krbetschek and Rieser, 1995; Baril and Huntley, 2003b). Varma et
443 al. (2013) observed phosphorescence with an intensity of ~35 % of the IR-RF signal (cf. Fig 2b
444 in Varma et al., 2013) immediately after irradiation up to 800 Gy. Phosphorescence caused by
445 irradiation can be a severe issue since IR-RF measurements need continuous irradiation during
446 signal measurement. Thus, phosphorescence superposition onto the main IR-RF signal can be
447 problematic and might be as high as 35 % of the IR-RF signal (Varma et al., 2013).
448 Nevertheless, if the phosphorescence intensity is independent of the previously administered
449 radiation dose, it might be neglected. In contrast, if the radiophosphorescence is dose-dependent,
450 it will be impossible to isolate it from the IR-RF signal. This possible superposition of IR-RF and
451 radiophosphorescence needs to be further investigated.

452 *Figure 7*

453 *(Phosphorescence)*

454 **5.4 IR-RF sensitivity**

455 Schilles and Habermann (2000) conducted a bleaching study on natural and commercially
456 available K-feldspar samples. Two repeated cycles of 20 h of sunlight bleaching resulted in
457 different IR-RF intensities and changes in the shape of the decay curve for each bleaching cycle.
458 Natural and commercial samples showed different bleaching levels and a relative change of
459 signal intensity of 3.6–4.8 % for natural sunlight and 5.1–8.9 % for artificial solar simulation
460 (SOL2, Hönle). These variations in signal intensity indicated sensitivity changes due to
461 bleaching and/or irradiation during the measurement. In order to cope with this, Schilles (2002)
462 suggested using a separate aliquot and measuring its IR-RF for two bleaching cycles. Based on
463 these additional measurements, a dimensionless correction factor could be derived from the ratio
464 of the regenerated IR-RF intensities (Fig. 8A).

465 Similarly, Varma et al. (2013) reported sensitivity changes during measurement and could not
466 recover a given dose using IR-RF. They derived a sensitivity correction factor F_S by repeating
467 the bleaching and regenerative IR-RF six times. F_S (also Sec. 6.1) is estimated from the ratio of
468 IR-RF intensity of the first regenerated cycle to the extrapolated intensity of the zeroth cycle
469 (Fig. 8B). Furthermore, Varma et al. (2013) recognized that all six sediment samples investigated

470 in their study needed a sensitivity correction to obtain reasonable dose recovery results. Erfurt
471 and Krbetschek (2003b) also showed a shape mismatch and change in intensity for multiple
472 measurements but demonstrated that this sensitivity change would only affect the dose
473 estimation by 3 % (cf. Fig 4 in Erfurt and Krbetschek, 2003b). In addition to these studies,
474 Buylaert et al. (2012) mentioned the possibility of a significant sensitivity change, either induced
475 by bleaching or by the IR-RF measurement itself.

476 Frouin et al. (2017) reported on a curve shape mismatch between the natural IR-RF (RF_{nat}) and
477 the regenerated IR-RF (RF_{reg}) curve (cf. Fig. 2 in Frouin et al., 2017), and rejected the measured
478 aliquots (Fig. 8C). In the literature, two attempts have been made to explain this behaviour:
479 Kreutzer et al. (2017) gave evidence that a technical artefact with the measurement equipment
480 caused an unwanted geometry change. Murari et al. (2018) investigated the possible reason for
481 this shape mismatch using three modern bleached samples in a dose recovery study. For these
482 samples, a given dose was recovered using the RF_{nat} and RF_{reg} signals. In their study, RF_{nat} refers
483 to IR-RF curves from the naturally bleached modern sample, and RF_{reg} refers to IR-RF curves
484 measured after bleaching with the solar simulator. As samples are bleached in both cases, both
485 IR-RF curves, RF_{nat} and RF_{reg} , can act as regenerated IR-RF curves. An offset of 23 % was
486 observed when the dose was recovered from the RF_{nat} signal (cf. Fig. 2 in Murari et al., 2018)
487 while all the samples were able to recover the known dose from the RF_{reg} signal with an
488 uncertainty of 4 %. Their findings showed the discrepancy in dose recovery and the mismatch of
489 the shape of RF_{reg} curves compared to RF_{nat} curves. The latter is attributed to the change in IR-
490 RF sensitivity. Possible causes for these sensitivity changes are the high photon flux of the built-
491 in solar simulator, the high laboratory dose rate and/or the interference from other neighbouring
492 peaks with the main IR-RF signal (i.e., 710 nm and 910 nm emissions; Trautmann, 1999; Erfurt
493 and Krbetschek, 2003b). In summary, it seems that IR-RF is affected by sensitivity changes that
494 should be monitored and corrected. Based on their findings, Murari et al. (2018) suggested a new
495 analysis and correction method named the '*horizontal and vertical correction*' method (Sec. 6.2).

496 **Figure 8**

497 **(Sensitivity change monitoring)**

498 5.5 IR-RF initial rise

499 A few IR-RF studies mentioned an unexpected signal rise at the beginning of the IR-RF
500 measurement (e.g., Schilles, 2002; Buylaert et al., 2012; Frouin, 2014; Huot et al., 2015; Frouin
501 et al., 2017). It was often described as a bump, a TL-like peak or an initial rise of the RF signal
502 (Fig. 9A; for further discussions on the dynamic range see below) and it typically persisted for
503 the first few hundred seconds (~6–12 Gy) before the IR-RF starts decaying monotonically (Huot
504 et al., 2015). According to Frouin et al. (2017), the initial rise in the natural signal seemed to be
505 positively correlated with the equivalent dose (D_e) (cf. Fig. S7 in Frouin et al., 2017) of a sample
506 and was observed for every K-feldspar sample used in their study.

507 In contrast, the Freiberg group never reported such IR-RF behaviour (e.g., Krbetschek et al.,
508 2000; Erfurt, 2003b) leading to speculation that differences in instrumental design (overall
509 system efficiency, different detection bandpass filter combinations or radiation source strengths)
510 may cause the effect or favour its detection. Measurements using both commercial devices
511 (*lexsyg research* and *Risø*, Sec. **Error! Reference source not found.**) showed the initial rise
512 behaviour (e.g., Huot et al., 2015; Frouin et al., 2017; Qin et al. 2018). However, this is not
513 discussed in detail by Buylaert et al. (2012) who discarded the signal corresponding to the first
514 ~20 Gy from their data analysis considering it as a sample-specific behaviour.

515 Huot et al. (2015) thoroughly investigated the origin of the initial rise after bleaching
516 (regenerated signal). They hypothesized that the rapid increase in RF observed at the beginning
517 of the irradiation, is not due to higher electron trapping, but can be explained by thermally
518 assisted phosphorescence. “Minute variations in sample temperature” (Huot et al., 2015, p. 241)
519 can cause this peak because of the existence of shallow traps which emit phosphorescence in the
520 near-infrared region. Their recommendation to avoid this peak was to wait at least 1 h after
521 bleaching, let the sample cool down to room temperature, or measure IR-RF at elevated
522 temperatures of around 70 °C to 100 °C. Nevertheless, the phenomenon does not seem to
523 disappear from the IR-RF signal even when measured at elevated temperatures of 70 °C and
524 waiting for one h after bleaching (cf. Fig. 2 vs Fig. 7 in Frouin et al., 2017).

525 Furthermore, the reported a correlation between the intensity of the initial rise in the natural
526 signal and the sample's D_e (cf. Frouin et al., 2017 their Fig. S7), indicated that shallow TL traps

527 alone cannot explain this phenomenon. Nevertheless, from the perspective of dating, it seems
528 that the effect of the initial rise does not affect dose estimation as it appears only for 100 s to 200
529 s (typically ~6–12 Gy) in every IR-RF signal (i.e., natural and regenerated IR-RF signals).
530 However, further investigations combined with modelling are needed to better understand the
531 origin of the IR-RF signal increase during the first seconds.

532 ***Figure 9***

533 ***(Initial rise and dynamic range)***

534 **5.6 IR-RF signal stability**

535 The IR-RF signal stability has two dimensions: thermal stability and athermal stability. The first
536 is directly related to the depth of the trap and represents the stability of the electrons captured by
537 the defect over time, dependent on the ‘burial’ temperature. The second, also known as
538 ‘anomalous fading’ (Wintle 1973), is temperature independent.

539 The thermal stability of the IR-RF signal was investigated by Trautmann et al. (1999a) who used
540 pulse annealing experiments, and they reported thermal stability of the IR-RF signal up to 450 °C
541 (Fig. 10A). However, this result was observed only for one sample (Ook1), which is >1 Ma old;
542 two younger samples showed a decrease in signal intensity after 250 °C (Fig. 10A). Later
543 experiments by Erfurt and Krbetschek (2003b) and Frouin et al. (2017) (Fig. 10B) confirmed
544 these findings. Further, it was noticed that for temperatures of 250 °C and higher, natural IR-RF
545 (RF_{nat}) signal intensities decreased with pulse annealing temperature (Fig. 10B) while they
546 increased slightly for regenerated IR-RF signals (RF_{reg}). If annealing at high temperatures resets
547 the IR-RF signal, the IR-RF intensity should not decrease, which is in accordance with
548 observations on RF_{reg} , but in contradiction to that for RF_{nat} . This contrasting feature may be
549 explained by a change of the IR-RF sensitivity with temperature. In thermoluminescence (TL)
550 studies on K-feldspar rapid, temperature-induced luminescence sensitivity decreases were
551 frequently reported (Aitken, 1985a, 1998). Those changes are non-repeatable in subsequent dose
552 cycles (cf. reasoning in Frouin et al., 2017).

553 Nevertheless, while temperatures above ca. 250 °C may impact the D_e , these observations should
554 not be used to draw general conclusions on the thermal stability of the defect responsible for the

555 IR-RF emission. Erfurt (2003a, b) referred to works on amazonite (cf. Ostrooumov, 2016 for an
556 overview) and argued that the Pb^{+} centres are stable up to $\sim 450^{\circ}C$ (Speit and Lehmann 1982) or
557 even up to $700^{\circ}C$ (assumption in Erfurt, 2003b: $500^{\circ}C$; $700^{\circ}C$ in Ostrooumov, 2016). Above
558 this temperature, the Pb^{+} centre disappears (a process also referred to as de-amazonitization).

559 Krbetschek et al. (2000) presented experimental results supporting the hypothesis of long-term
560 stability of the IR-RF signal. For instance, short-term (days to months) fading tests with storage
561 of samples for several months at room temperature showed no sign of signal increase (i.e., no
562 emptying of traps) which seems to confirm signal stability over short periods (at room
563 temperature). Furthermore, based on the dating of sediment samples using IR-RF, e.g., Wagner
564 et al. (2010) and Novothny et al. (2010) claimed that the IR-RF signal exhibited no indication of
565 fading for ages in the range ca 420–700 ka (Wagner et al., 2010) and 148–250 ka (Novothny et
566 al., 2010). Likewise, Frouin et al. (2017) and Kreutzer et al. (2018a) reported a good agreement
567 with the independent age control of even older ages. By contrast, Buylaert et al. (2012) showed
568 age underestimation for older samples (>100 ka) and overestimation for younger samples (< 50
569 ka). They speculated whether the offset could be explained by signal instability (fading),
570 bleachability and sensitivity change during measurement. They also showed the natural IR-RF
571 signal from an infinitely old sample was only 84 % of the saturation, suggesting the signal might
572 fade. However, the measurement setup by Buylaert et al. (2012) did not match the suggestions by
573 Erfurt and Krbetschek (2003b), e.g., regarding the detection window, and should be read
574 cautiously. Recently, Kumar et al. (2021) reinterpreted the findings by Buylaert et al. (2012).
575 They reported IR-PL age results in agreement with independent age control. These findings
576 indicate that IR-PL does not suffer from athermal fading or signal instability. However, since
577 Kumar et al. (2018) hypothesised a similar trap for the IR-PL and the IR-RF, they concluded that
578 IR-RF does not suffer from signal instability. Hence, without presenting new IR-RF data, Kumar
579 et al. (2021, p. 14) concluded: “[...] *that the under-estimation in IR-RF [meant are the results*
580 *reported by Buylaert et al., 2012] is likely because of sensitivity changes rather than signal*
581 *stability.*” Nevertheless, beyond the research summarized above, further studies should be carried
582 out to investigate the thermal and athermal stability in the context of IR-RF as a luminescence
583 dating method. For IR-PL, Kumar et al. (2021) suggested tests on geological samples (\sim Ma), i.e.

584 samples in apparent dose saturation, which might also provide a good test for the IR-RF signal
585 stability in future studies.

586 **Figure 10 A B**

587 **(Signal stability)**

588 **5.7 IR-RF dose limits**

589 The minimum measurable dose has not yet been systematically determined with IR-RF. While
590 Erfurt (2003b) estimated a dose of ca 40 Gy, Frouin et al. (2017) reported measurable doses of
591 0.5 ± 1.0 Gy and 1.2 ± 1.9 Gy for two modern analogue samples. Current instrument
592 configurations allow signals with a few photon-counts per second to be distinguished. In
593 available luminescence measurement systems (Sec. 3), the IR-RF signal of K-feldspar is usually
594 of the order of a million photon counts per second with signal intensities at its maximum when
595 the sample is bleached, i.e., for zero dose samples. Thus, the minimum measurable dose (limit) is
596 a function of stimulation dose-rate (Gy s^{-1}), the measurement channel resolution (s channel^{-1}) and
597 the applied statistical procedure to distinguish two bright signals and determine the D_e (e.g., the
598 sliding method causes discretization effects, Sec. 6.2). For example, a sampling rate as applied
599 by Murari et al. (2018) of $10 \text{ s channel}^{-1}$ for a dose rate of ca. 0.06 Gy s^{-1} would theoretically
600 correspond to a minimum distinguishable dose of 0.6 Gy on average.

601 The IR-RF dynamic range is defined as the ratio of the maximum to the minimum of the IR-RF
602 signal intensity. In other words, this is the ratio of the IR-RF signal from saturation to the
603 bleaching level of the sample, which in general varies about a factor of 2 (Erfurt and Krbetschek,
604 2003a). The IR-RF signal dynamic range is minimal (Fig. 9B) compared to the signal dynamics
605 from the other variants of luminescence such as OSL or IRSL, where it typically is at least an
606 order of magnitude higher. Due to low signal dynamic ranges, the slope of IR-RF intensity (I)
607 with respect to dose (D_e) changes gradually and finally approaches zero. In terms of resolving
608 dose estimates, the resolution becomes impoverished in the higher dose region as a slight change
609 in intensity (dI) may lead to a large uncertainty in dose estimation (dD_e). Erfurt and Krbetschek
610 (2003b) recommended determining the dose where the slope of signal intensity vs dose
611 approaches a value of zero (i.e., $dI/dD_e \approx 0$). Based on this parameter, they found that for their
612 reader configuration, IR-RF curves allow dose estimation up to ~650 Gy.

613 However, the upper dose limit of IR-RF, and with it, the temporal range, is subject to ongoing
614 research. Krbetschek et al. (2000) reported a saturation D_e value of $1,440 \pm 215$ Gy (nature of the
615 error not reported) for a single sample, and in a recent IR-RF dating study Kreuzer et al. (2018a)
616 reported a measurable mean dose of $1,064 \pm 41$ Gy (mean \pm standard deviation). Erfurt (2003b)
617 estimated a mean saturation dose as high as 1,500 Gy. However, Erfurt (2003b) and Erfurt and
618 Krbetschek (2003b) also estimated the maximum resolvable dose at 600 Gy to 650 Gy as the
619 small IR-RF signal dynamic range can limit the precision of signal interpolation. The highest,
620 single aliquot, IR-RF dose of $4,181 \pm 371$ Gy (mean \pm standard deviation) was reported by
621 Wagner et al. (2010) (cf. their “Supporting Information”, Table S2) using the same instrument as
622 Erfurt et al. (2003).

623 On a *lexsyg research* system Frouin et al. (2017) recently reported successful measurement of a
624 $\sim 2,100$ Gy dose using a regenerated IR-RF signal that was recorded up to 4,000 Gy cumulative
625 dose (cf. their Fig. 7 for sample TML1). Furthermore, Murari et al. (2018) demonstrated accurate
626 laboratory dose recovery up to 3,600 Gy by interpolating onto a regenerated IR-RF curve
627 measured up to 3,900 Gy. However, it should be pointed out that the intensity difference between
628 2,000 Gy and 3,500 Gy was only around 4 % (Fig. 9B for the dynamic range of IR-RF), which
629 leaves the results susceptible to minimal intensity changes. Hence, at this moment, we cannot
630 refer to a saturation limit of IR-RF. However, the one single value published by Murari et al.
631 (2018) of ca. 3,600 Gy would allow age determinations (dose rates in the order of 2–3 Gy ka⁻¹)
632 of 1.2 Ma to 1.8 Ma. Whether this dose (and temporal) range is feasible for routine dating is still
633 under debate.

634 **5.8 The IR-RF alpha-efficiency**

635 The ionisation efficiency and, with it, the efficiency of induced luminescence per unit dose,
636 depends on the type of irradiation (i.e., α - vs β - vs γ -radiation). Commonly, the luminescence
637 produced by α -particles per unit dose is substantially lower than for β - or γ -radiation. Thus, the
638 α -efficiency needs to be determined to correctly calculate the β -equivalent α -dose rate
639 contribution (cf. Aitken, 1985a) if polymineral fine grain (4–11 μm) or other grain size fractions
640 untreated with HF are used. So far, only a single study exists determining the α -efficiency of K-
641 feldspar using IR-RF. Kreuzer et al. (2018b) used an α -flux calibrated ²⁴¹Am source. The central

642 S_α -value (Guérin and Valladas, 1980; Valladas and Valladas, 1982) obtained from four fine-
643 grain K-feldspar samples (84 aliquots) was $9.26 \pm 1.62 \mu\text{Gy}/(10^3\alpha \text{ cm}^{-2})$. The corresponding
644 (dimensionless) value in the a -value system (cf. Aitken 1985b) of 0.067 ± 0.012 is similar to a -
645 values reported for IRSL polymineral fine grain (e.g., Kadereit et al., 2010). Based on these
646 findings and if the α -efficiency cannot be determined, an estimated a -value of 0.07 ± 0.01
647 (applied to fine grain and unetched coarse grains, cf. Kreutzer et al., 2018b) appears to be
648 justified.

649 **6 Measurement protocols and data analysis**

650 Like other luminescence measurement protocols for equivalent dose (D_e) determination (e.g., for
651 TL, OSL or IRSL), over the years, several measurement protocols and data analysis techniques
652 have been proposed to determine the D_e for IR-RF.

653 **6.1 IR-RF measurement protocols**

654 The first comprehensive IR-RF measurement protocol named IRSAR (infrared single-aliquot
655 regenerative-dose) was presented by Erfurt and Krbetschek (2003b). Frouin et al. (2017)
656 introduced a modified version of this protocol and entitled it RF₇₀ (where the subscript '70' refers
657 to the applied measurement temperature of 70 °C). Additionally, several other protocols have
658 been reported in the literature and are summarized in Table 6.

659 **Table 6**

660 **(Measurement protocols)**

661 All listed protocols consist of less than six measurement steps. Common to all protocols are three
662 main steps: (I) measurement of the natural IR-RF signal (RF_{nat}), (II) signal resetting by bleaching
663 and (III) measurement of the regenerated IR-RF (RF_{reg}) signal after bleaching. The duration of
664 the IR-RF measurements (natural, regenerative) is determined by the chosen data analysis
665 approach (Fig. 11). For example, D_e determination via curve fitting and signal extrapolation
666 results in IR-RF measurements of longer duration for the natural IR-RF signal than for the
667 regenerated signal and vice versa for a D_e determination via interpolation.

668 Trautmann et al. (1999a), Krbetschek et al. (2000) and Schilles (2002) distinguished between an
669 additive (extrapolation) and a regenerative (interpolation) measurement approach, depending on
670 the particular IR-RF signal (natural: additive; regenerative: regenerative) used for subsequent
671 curve fitting. However, this distinction is misleading and should be avoided as it conflicts with
672 the commonly accepted terminology used for TL/OSL. All recorded IR-RF signal curves are
673 dose-response curves, and signal resetting is carried out by optical bleaching. Thus, natural IR-
674 RF curves are always additive dose-response curves, irrespective of the technique used to
675 analyse the data and to obtain the D_e , namely: extrapolation, interpolation or sliding (see the
676 following section).

677 *Bleaching duration:* All published protocols include an optical bleaching step to reset the natural
678 IR-RF signal. The bleaching is either carried out by using an artificial light source or by natural
679 sunlight. To mimic natural sunlight conditions, Frouin et al. (2015) proposed a bleaching
680 spectrum consisting of six different wavelengths ranging from UV-A (365 nm) to NIR (850 nm),
681 while Buylaert et al. (2012) used only a single wavelength (UV-violet LED, 395 nm) to reset the
682 IR-RF signal. The bleaching duration is sample dependent and linked to the technical
683 specification of the equipment, the available wavelengths, and power. Using a similar
684 measurement setup, Varma et al. (2013) and Buylaert et al. (2012) found bleaching for 800 s and
685 1,500 s respectively, to be sufficient for most cases, Frouin et al. (2017) suggested solar
686 simulator bleaching for at least 10,800 s. Kreuzer et al. (2018a) suggested a bleaching test using
687 the internal solar simulator of their *lexsyg* system. The test applied consecutive bleaching steps
688 of 1,000 s each. A stable signal plateau indicates sufficient bleaching. Generally, it appears that
689 longer bleaching times should be preferred to ensure the resetting of the natural IR-RF signal.
690 For further details on the bleaching behaviour of the IR-RF signal see Sec. 5.2.

691 *Pause duration:* Five out of seven IR-RF protocols (Table 6) suggested a pause after the optical
692 resetting of the IR-RF signal for at least 1,800 s. The pause is believed to account for an
693 unwanted superposition of IR phosphorescence on the IR-RF signal (e.g., Erfurt and Krbetschek,
694 2003b). Varma et al. (2013) carried out the pause as a phosphorescence measurement just before
695 the stimulation itself. Based on their results, it appears that the phosphorescence is induced only
696 by the irradiation ('radiophosphorescence') and that it is not further increased by bleaching. They
697 thus proposed an optimum bleaching time of 800 s to reduce phosphorescence to its residual

698 level without implementing an additional pause within the measurement procedure. However,
699 this study contradicted the observation made on the same system (*Risø* TL/OSL DA-20 with IR-
700 RF attachment) by Buylaert et al. (2012) who showed the appearance of IR phosphorescence
701 even after bleaching of 1,500 s, though it was two orders of magnitude smaller than the IR-RF
702 signal which can probably be considered negligible. Nevertheless, other studies contradicted
703 these findings, e.g., Erfurt (2003b), Erfurt and Krbetschek (2003b) and Huot et al. (2015) showed
704 the presence of phosphorescence directly emitted after bleaching. The above-described
705 observations suggest that an additional pause of 30 min up to 1 h might be beneficial to minimize
706 the potential effects of unwanted signal superposition from the phosphorescence caused by
707 bleaching (also Sec. 5.3).

708 *Preheat and measurement temperature:* The work of Trautmann (1999) gave evidence for a
709 strong temperature dependence of the IR-RF signal of K-feldspar, which appears to be related to
710 the sample's age (see also Erfurt, 2003b). Considering the dependency of the IR-RF signal
711 intensity (Trautmann, 1999; Erfurt, 2003b; Frouin, 2014) on the preheat and measurement
712 temperature, measurements under well-controlled temperature conditions appear advisable.
713 However, due to technical limitations, measurements under controlled (elevated) temperature
714 conditions have only been applied by Frouin et al. (2017). They suggested a preheat of 70 °C
715 based on the observation of thermally assisted phosphorescence. Huot et al. (2015) advised that a
716 temperature range of 70 °C to 100 °C would be suitable. However, Erfurt and Krbetschek
717 (2003b) neglected the need for any preheat prior to measurement following their observation of
718 no change in IR-RF intensity from room temperature to 250 °C (cf. Fig. 2 in Erfurt and
719 Krbetschek, 2003b). Nevertheless, a comparison of IR-RF ages with independent age control
720 showed improvement in results when measurements are carried out at elevated temperature
721 (Frouin et al., 2017). Therefore, Frouin et al. (2017) recommended measurements at elevated
722 temperature.

723 *Sensitivity correction (also Sec. 5.4):* Monitoring changes in the dose-response characteristics is
724 an essential feature of every OSL SAR protocol. Schilles (2002) and Varma et al. (2013)
725 included treatments to correct for unwanted changes in IR-RF signal sensitivity by introducing a
726 correction factor for IR-RF measurements. Murari et al. (2018) investigated a new way of
727 correction. In this method, the shapes of IR-RF curves are matched by moving the RF_{nat}

728 vertically along with horizontal sliding (Sec. 5.4 for sensitivity change). This method was able to
729 recover a given dose with 3–10 % accuracy, compared to an offset by 15–23 % when recovered
730 only using the horizontal sliding method proposed by Buylaert et al. (2012). The recommended
731 method (Kreutzer et al., 2017; Murari et al., 2018) does not need any extra measurements other
732 than those implemented in the protocol suggested by Frouin et al. (2017). However, the RF_{nat}
733 measurement should be long enough to produce an RF signal with pronounced curvature to
734 match the RF_{nat} and RF_{reg} curves.

735 **6.2 Data analysis**

736 Data analysis for D_e estimation is essential for age determination. D_e determination requires a
737 comparison of the natural and a minimum of one regenerated IR-RF signal. The different
738 methods available for making this comparison are described below.

739 *Figure 11*

740 *(D_e determination methods)*

741 *Extrapolation and Interpolation method:* Three different approaches were presented to analyse
742 IR-RF data (Fig. 11): (I) extrapolation, (II) interpolation and (III) sliding. The first two
743 approaches comprise a mathematical curve fitting for D_e determination. Extrapolation (Fig. 11A)
744 and interpolation (Fig. 11B) requires that either the natural or regenerative signal is recorded
745 over a more extended period (natural signal: extrapolation; regenerative signal: interpolation).
746 The chosen channel resolution and stimulation time determine the precision of the curve fitting
747 and thus, the statistical error of the D_e . For curve fitting (extrapolation, interpolation), Trautmann
748 et al. (1999a), Krbetschek et al. (2000) and Schilles (2002) proposed a single exponential
749 decaying function with three parameters. Later, Erfurt and Krbetschek (2003b) recognized that
750 the curve shape could be best described using a so-called stretched exponential function (Fig.
751 12). This function was suggested in a general form by, e.g., Pavesi and Ceschini (1993). The
752 stretched exponential function introduces a dispersion factor (β), which accounts for the
753 underlying physical processes in disordered condensed matter systems. Unfortunately, the
754 mathematical expression of this function type is not consistent in the IR-RF literature (Fig. 12)
755 and differs regarding the placement of β in the equation. Although the functions shown in Fig. 12
756 may result in consistent D_e estimations, they reveal different curve shapes for similar parameter

757 sets. Therefore, parameters describing an IR-RF curve's decay cannot be compared without a
758 statement on the applied mathematical expression.

759 **Figure 12**

760 **(Equations used for IR-RF curve fitting)**

761 Due to the general difficulties associated with D_e estimation by extrapolation (i.e., substantial
762 uncertainties), this methodological approach appears to have been abandoned in later studies, and
763 more recently only D_e estimation by interpolation has been applied (e.g., Wagner et al., 2010;
764 Novothny et al., 2010; Kreutzer et al., 2014). Nevertheless, every fitting method requires an
765 assumption regarding the IR-RF curve shape, either based on a model or the best graphic
766 adaption of the curve shape. Furthermore, IR-RF curves recorded only for a short time do not
767 sufficiently reveal the curve shape and potential changes.

768 *Sliding method:* Buylaert et al. (2012) suggested a data analysis method based on horizontal
769 sliding of the RF_{nat} curve until the best match is reached (inspired by the *Australian slide* method
770 introduced initially by Prescott et al., 1993). This approach appears to be even more justified
771 since Frouin et al. (2017) pointed out an initial rise at the beginning of the natural IR-RF curve
772 (Sec. 5.5). The observed initial rise at the beginning of the IR-RF curve does not allow an
773 unbiased channel selection if curve fitting combined with interpolation or extrapolation is
774 applied. In other words, for IR-RF data analysis, the (horizontal) sliding technique should be
775 favoured over the curve fitting approach. However, it was often seen that RF_{nat} and RF_{reg} curves
776 did not match after horizontal sliding. Kreutzer et al. (2017) suggested enhancing the technique
777 by combining vertical and horizontal sliding to account for an observed IR-RF light level change
778 encountered for a particular technical setup, presented in Murari et al. (2018). The sliding
779 method requires a long natural IR-RF measurement to match the regenerative IR-RF, e.g., Frouin
780 et al. (2017) (their supplement) recommended a minimum of 40 channels for robust D_e
781 estimation for the horizontal sliding method. In the case of the vertical and horizontal sliding
782 methods, Murari et al. (2018) used 100 channels. However, the precise number depends on the
783 signal shape.

784 *Error estimation:* Krbetschek et al. (2000) suggested that the primary source of random error in
785 the IR-RF 'mean' D_e arises from changes in the sample geometry at a single-grain level (see also

786 Trautmann et al., 2000b). In contrast to OSL, where the dose-response curve is typically
787 reconstructed with a few (e.g., 5–15) regenerative dose measurements, the number of channels
788 used for constructing the IR-RF dose-response curve can be increased dramatically (e.g., >1,000
789 values) and is limited only by the instrumental signal-to-noise ratio and the total number of
790 allowed channels by the system. Consequently, for IR-RF dating studies, individual (statistical)
791 errors have been ignored, and the standard error deduced from individual D_e distributions (e.g.,
792 Wagner et al., 2010; Lauer et al., 2011; Kreutzer et al., 2014). To account for potential errors
793 Frouin et al. (2017) (their supplement) developed an approach to estimate the standard error of
794 an individual aliquot based on a non-parametric bootstrapping approach (Efron, 1979) for the
795 sliding method. Nevertheless, the results of Frouin et al. (2017) also showed that the obtained
796 individual statistical standard error remains negligible in comparison to inter-aliquot scatter and
797 becomes relevant only for dim IR-RF signals.

798 *Data analysis software:* To analyse IR-RF data, no specialized software is needed, and
799 commercial software solutions, e.g., *SigmaPlotTM* or *ORIGINTM* may be sufficient to analyse
800 single measurements. However, within a dating study, the amount of data may demand more
801 comprehensive and efficient solutions. Two freely available software solutions have been
802 published to analyse IR-RF data based on the IRSAR Erfurt and Krbetschek (2003b) approach.
803 The *MS WindowsTM* software *RLanalyse* (Lapp et al., 2012; latest version 1.20) has implemented
804 the (horizontal) sliding method and works with BIN/BINX-files produced by a *Risø* TL/OSL
805 reader. The most recent version of the function `analyse_IRSAR.RF()` implemented in the
806 package ‘Luminescence’ (Kreutzer et al., 2012, 2018c) makes use of the platform-independent
807 programming language **R** (R Core Team, 2018), and supports the horizontal and vertical sliding
808 approach. The function also supports D_e estimation via curve fitting as described by Erfurt and
809 Krbetschek (2003b) as well as via sliding including the individual standard error estimation
810 approach described in Frouin et al. (2017) and Murari et al. (2018). Through the ‘Luminescence’
811 environment, XSYG-files (Freiberg Instruments *lexsyg* readers), BIN/BINX-files (*Risø* TL/OSL
812 reader) as well as various other data formats (e.g., file endings *.csv, *.txt) are supported as input
813 data.

814 **7 Application of IR-RF dating**

815 The broader use of IR-RF as a dating method for sediments started mainly after introducing the
816 IRSAR protocol by Erfurt and Krbetschek (2003b). Signal saturation levels of > 1,000 Gy (e.g.,
817 Erfurt and Krbetschek, 2003b and Sec. 5.7) favoured IR-RF dating applications on Middle
818 Pleistocene sediments which are generally beyond the quartz OSL dating limit. The typical dose
819 saturation for quartz OSL measured in the UV is reached around 150–200 Gy (Wintle and
820 Murray, 2006) except for a few cases where quartz doses >300 Gy are reported (e.g., Lowick and
821 Valla, 2018). Until now, IR-RF dating has mainly been applied to coarse grain K-rich feldspar
822 using multiple-grains (Secs. 7.17.2). Spatially resolved and single grain studies are limited to
823 preliminary work (e.g., Schilles 2002; Trautmann et al., 2000b) and a manuscript in an open
824 discussion by Mittelstrass and Kreutzer (preprint) and are thus not further discussed here.
825 Applications of IR-RF on polymineral fine-grain samples (4–11 μm) are currently limited to
826 three studies (Schilles, 2002; Kreutzer et al., 2018b; Coussot et al., 2019).

827 **7.1 Application to glacio-fluvial and fluvial sediments**

828 In the past, IR-RF dating has been favoured particularly for constraining the timing of the
829 Saalian glacial cycle and the Eemian interglacial by dating fluvial deposits of sites located in
830 Central/Eastern Germany (Eissmann, 2002) by Degering and Krbetschek (2007), Krbetschek et
831 al. (2008) and Kreutzer et al. (2014). Degering and Krbetschek (2007) presented IR-RF ages
832 ranging from 120 ± 15 ka to 158 ± 21 ka for the Eemian site Klinge (Germany), and the results
833 were in good agreement with quartz and K-feldspar OSL and IRSL luminescence dating results.
834 IR-RF dated fluvial sites (e.g., Wallendorf and Delitzsch, Germany) are highly relevant for
835 establishing a chronology for Middle Pleistocene Palaeolithic human activity in Europe due to
836 the presence of stone-artefacts embedded in fluvial sands and gravels. Krbetschek et al. (2008)
837 presented IR-RF ages ranging from ~150 ka to ~306 ka for the Saalian period and highlighted
838 human activity in Central Germany already at around 300 ka. Lauer and Weiss (2018) compared
839 pIRIR₂₉₀ luminescence ages from the important palaeolithic site of Markkleeberg (Baumann et
840 al., 1983; Schäfer et al., 2003) with previously available IR-RF ages (Krbetschek et al., 2003)
841 and found the pIRIR₂₉₀ and IR-RF ages were in excellent agreement and provided late MIS 6
842 ages for the upper fluvial sequence at the site. Also, for the key site of the Homo heidelbergensis,

843 located at Mauer in south-west Germany, IR-RF was applied to fluvial deposits correlated to the
844 archaeological horizon of the Mauer mandible. At this site, the IR-RF ages were in good
845 agreement with results of combined electron spin resonance (ESR)/U-series dating on mammal
846 teeth, yielding an age of around 0.6 Ma (Wagner et al., 2010). Lauer et al. (2011) used IR-RF to
847 date fluvial deposits collected from sediment-cores drilled into the northern Upper Rhine Graben
848 (Germany). They deduced several fluvial aggradation periods and phases of increased tectonic
849 subsidence between ~300 ka and ~650 ka based on these IR-RF ages. Li et al. (2017) compared
850 the data reported by Lauer et al. (2011) with their chronology based on fading corrected pIRIR₂₂₅
851 ages obtained for the core Heidelberg UniNord 1. Except for the lowermost sample (below the
852 B/M boundary) both chronologies were broadly consistent. For the lowest sample, Li et al.
853 (2017) reported a minimum age of $>602 \pm 77$ ka, consistent with the magnetostratigraphic
854 information which was not available in 2011. In light of the new findings, the IR-RF age of 643
855 ± 28 ka by Lauer et al. (2011) should be considered as minimum age. The reasons for this age
856 underestimation should be subject to future research.

857 In general, studies presented by Krbetschek et al. (2008) and Wagner et al. (2010) demonstrated
858 good agreement with independent age control. In contrast to these studies, Buylaert et al. (2012)
859 showed that IR-RF dating results of coastal marine sediments from Russia and Denmark as well
860 as colluvial sediments from France were either overestimated (for ages between 20–45 ka) or
861 underestimated (for older samples ~128 ka) compared to independent dating methods based on
862 biostratigraphy, radiocarbon (¹⁴C), OSL and pIRIR₂₉₀ (for numerical values cf. Table S1 in
863 Buylaert et al., 2012).

864 *Figure 13 ABC*

865 *(Age comparison)*

866 **7.2 Application to aeolian deposits**

867 Well-bleached sediments, such as wind-blown loess or dune sands seem to be most suitable for
868 IR-RF dating applications, although the amount of sand-sized K-feldspars in silt-dominated loess
869 is limited. Early aeolian samples used for IR-RF dating result originate from a sediment core
870 from the Gaxun Nur Basin in North-West Chin (Wünnemann et al., 2007). The IR-RF dating

871 results² significantly overestimated previously reported TL/IRSL ages and were discarded by the
872 authors (Wünnemann et al., 2007), without presenting further technical details.

873 Novothny et al. (2010) were the first to extract coarse-grained K-feldspars from Hungarian loess
874 for IR-RF dating. The IR-RF ages of ~200 ka presented by Novothny et al. (2010) significantly
875 overestimated the fading-corrected IRSL ages of ~130 ka, explained due to insufficient bleaching
876 of the coarse-grained fraction. An IR-RF age overestimation compared to quartz OSL ages of
877 reworked aeolian sediments from Egypt was also reported by Buylaert et al. (2012), which was
878 either attributed to a preliminary determination of the bleaching level before the regenerative
879 dose measurement or sensitivity changes between the measurement of the natural and
880 regenerated curves.

881 It was recently demonstrated that the modified IRSAR-protocol, measuring the IR-RF signal at
882 70 °C (RF₇₀), recovered IR-RF ages on modern aeolian samples that agreed with independent
883 age control. Frouin et al. (2017) have shown reasonable agreement with independent age control
884 from polymineral (4–11 µm) fine-grain results published by Meszner et al. (2013). However,
885 they also observed a large scatter in their D_e distributions. Another age from a loess sample from
886 the same site appeared to be underestimated. This offset was explained by the low D_e values
887 resulting from low signal intensities (Frouin et al., 2017).

888 Kreutzer et al. (2018a) presented a dating application study on coastal dynamics from the Médoc
889 region (south-west France), comparing coarse grain K-feldspar IR-RF ages (RF₇₀ protocol) with
890 quartz OSL ages and quartz multiple-centre ESR dating (Toyoda et al., 2000). In this study, the
891 IR-RF ages were systematically older than the SAR quartz ages, which was believed to be a
892 consequence of insufficient resetting of the IR-RF signal. However, this study showed
893 reasonable agreement with the ESR ages for older sediments (200–330 ka). Similarly, Scerri et
894 al. (2018) also found that RF₇₀ and pIRIR₂₉₀ age estimates were consistent within a 2-sigma limit
895 and in stratigraphic order. The aeolian samples from an archaeological site in Saudi Arabia
896 resulted in age estimates of ~276 ka for the older (archaeologically sterile) layer and 197 ka for
897 the human occupation layer.

² In Fig. 22.3 (Wünnemann et al., 2007) the IR-RF results were erroneously presented as OSL dates.

898 **7.3 Remarks on IR-RF age accuracy and independent age control**

899 Figure 13 presents a non-exhaustive overview of published IR-RF data. The ages from the IR-RF
900 dating approaches generally show good agreement with independent age control (e.g., Degering
901 and Krbetschek, 2007), whereas the IR-RF ages from Buylaert et al. (2012) disagree with
902 independently derived ages. Again, a good agreement between IR-RF and independent ages was
903 reported using a modified IRSAR protocol (RF₇₀) suggested by Frouin et al. (2017).

904 The study by Frouin et al. (2017) was the first to present various IR-RF dating applications with
905 a modified IRSAR protocol (RF₇₀), which agreed with independent age control. IR-RF dating of
906 a Pleistocene beach deposit from Peru and colluvial deposits from France appeared to be
907 overestimated compared to independent age information from IRSL, U/Th series or radiocarbon
908 dating; a pattern also observed by Schaarschmidt et al. (2019). However, for the Peruvian
909 sample, IR-RF and pIRIR₂₉₀ ages agreed within error limits. Similarly, Holocene beach sand
910 from Denmark and another colluvial example from France yielded ages in good agreement with
911 independent age information. In conclusion, published IR-RF dating results indicated that the IR-
912 RF dating method produced correct ages in some cases, but fails for other cases. It seems that
913 there are still methodological problems related to IR-RF dating, and further investigation is
914 needed to overcome these challenges.

915 **8 Summary and future directions of IR-RF dating**

916 Overall, regardless of ambivalent dating results in some studies, IR-RF appears to be a promising
917 but somewhat overlooked dating method on K-feldspars. The status quo renders a picture with
918 several, potentially, game-changing advantages but without a significant breakthrough because
919 those benefits are not received as significant enough by dating practitioners. On the other hand,
920 IR-RF poses a bunch of open questions and challenges that are yet to overcome.

921 **8.1 The status quo**

922 The plus side of IR-RF dating has different dimensions. From a **methodological perspective**,
923 IR-RF is believed to monitor the trapping of electrons in the principal trap, i.e., it is a *direct*
924 measurement of the dose accumulation in the mineral. This approach is conceptionally different
925 from conventional OSL, IRSL and TL measurements, involving secondary recombination

926 processes to infer the signal of interest. Debated methodological issues, such as phosphorescence
927 and sensitivity change (see Secs. 5.35.4), appear to be manageable by proper experimental and
928 data analysis design.

929 From a **practical perspective**, compared to post-IR IRSL dating, for instance, the measurement
930 sequence for one aliquot is reasonably concise, less error-prone, and, depending on the aimed
931 dose range, likely less time-consuming (depending on the chosen measurement sequence). The
932 dose-response curve is the IR-RF curve measured during irradiation with a resolution usually in
933 the order of a fraction of a Gy. Instead of applying different fitting equations determining the D_e ,
934 the data analysis using the sliding method, i.e., matching two dose-response curves (RF_{nat} and
935 RF_{reg}), could not be more straightforward. Software to analyse IR-RF signals is freely available
936 and partly open-source. The biggest obstacle for applying IR-RF dating in the past, availability
937 of equipment, is no more. At least two commercial manufacturers offer ready-to-use IR-RF
938 readers for research and dating applications.

939 From a **dating perspective**, the target mineral, K-feldspar, shows a high natural abundance, an
940 acknowledged higher luminescence dating range compared to quartz, and the internal potassium
941 concentration lowers the impact of the external dose-rate contribution. However, conventional
942 feldspar luminescence is reported to suffer from an unwanted athermal signal loss (fading).
943 Contrary to IRSL, no definite evidence was provided for fading of the IR-RF signal of K-
944 feldspars to date. Although Buylaert et al. (2012) reported age underestimations for older
945 samples of ca 30 %, this does not appear to be a generally observed pattern. Furthermore, signal
946 instability as a cause for this observation was considered unlikely by Kumar et al. (2021). The
947 thermal stability of the IR-RF signal (determining the potential age range) appears to be
948 sufficiently high up to 700 °C (Sec. 5.6), though previous experiments indicated changes of the
949 IR-RF signal shape above ~250 °C (Trautmann et al., 1999a; Erfurt and Krbetschek, 2003b;
950 Frouin et al., 2017).

951 However, to sustain, a dating method has to show advantages over established methods, which
952 are also perceived as significant for application studies. Supposing that the signal of choice is
953 thermally and athermally stable, for luminescence-based chronologies such advantages are
954 measured in terms of bleachability and temporal range.

955 Compared to pIRIR₂₉₀, which seems to suffer from no or at least less fading than IRSL, IR-RF's
956 bleachability is comparable. In other words, in natural environments involving sediment
957 transport processes with only short sunlight exposure, IR-RF dating seems to be as applicable as
958 pIRIR₂₉₀ and other methods may suit better. Whether the temporal range is as high as the ~1.2–3
959 Ma (~ 3,600 Gy) postulated by Murari et al. (2018) is yet to be revealed. More realistically seem
960 values around up to 1,500 Gy measured by, e.g., Erfurt (2003b), Frouin (2014), Frouin et al.
961 (2017) and Kreutzer et al. (2018). Here we conclude that the signal saturation limit (and thus the
962 temporal range) appears to be significantly higher than for conventional OSL on quartz (up to
963 400 Gy, typically lower, for a review cf. Wintle and Adamiec, 2017). This “winning margin” is
964 less pronounced if IR-RF is compared to studies reporting post-IR IRSL (more specific:
965 pIRIR₂₉₀) or MET-pIRIR results. For instance, Liu et al. (2016) reported doses up to ca. 1,240
966 Gy, however, ages were reported to underestimate the independent age control above ca. 600–
967 900 Gy (cf. Lieu et al., 2016; their Table 2 and Fig. 3). For MET-pIRIR, Li et al. (2014) reported
968 potential natural dose measurements up to ca. 1,500 Gy, however, it remains unclear whether
969 such values can be met regularly in routine dating studies (cf. Zhang and Li, 2020 for a
970 discussion).

971 **8.2 Future directions**

972 Future methodological research on IR-RF should first resolve some open debates, particularly on
973 signal saturation and signal stability (fading). Although fading does not appear to be a generally
974 observed pattern, this topic should be explored in more detail, along with potential sensitivity
975 changes using samples of known and geological age. The biggest obstacle to resolving whether
976 the signal recorded with IR-RF is stable or suffers from an athermal signal loss over geological
977 timescales might be the experimental design. From the current perspective, it appears that short
978 experiments over a couple of weeks to months are not sufficient to provide answers to that
979 question. Hence, research should involve laboratories with a relatively long history and an
980 archive of already measured, irradiated and stored feldspar specimen. The quantification of the
981 saturation level is more of theoretical than practical relevance.

982 With regard to the literature, it is safe to assume a rather broad, sample dependent, saturation
983 level range between 600 Gy and 2,000 Gy up to perhaps 4,000 Gy. However, of relevance for the

984 dating practice is the limit of the K-feldspar sample at hand, regardless of any theoretical value.
985 In other words, the saturation level of IR-RF dating and with it the temporal range, will itself
986 establish circumstantially over time; with or without dedicated research. However, both research
987 on the fading behaviour and the signal saturation might contribute to a broader understanding of
988 the physics underpinning IR-RF. To date, Trautmann's model (Trautman et al., 2000a) remained,
989 to our knowledge, the only comprehensible model genuinely dedicated to IR-RF. Clearly, efforts
990 are needed to combine the old and new findings around IR-PL and combine them with
991 established knowledge in IRSL to decipher the proposed resemblance of IR-RF and IR-PL (cf.
992 Kumar et al., 2020). Similarly, while there seems to be extensive research to identify the defect
993 responsible for IR-PL (most recently Kumar et al., 2020), it appears that established knowledge
994 on the role of Pb in the luminescence production in feldspar (cf. textbook by Ostrooumov, 2016)
995 did not (yet) receive full attention.

996 On the application site, the next logical application step is spatially resolved IR-RF in a single
997 grain (Mittelstrass and Kreutzer, preprint) or even sub-grain level as concluded by Kumar et al.
998 (2020).

999 Another direction to test, for already available multi-grain IR-RF, are fine-grain (polymineral)
1000 mineral fractions. The few attempts reported in the literature yielded promising results (Schilles
1001 2002; Coussot et al., 2019). However, the mixture of minerals in such samples may hamper its
1002 application. Meyer et al. (2013) used quantitative evaluation of minerals by scanning electron
1003 microscopy (QEMSCAN) for polymineral fine grain OSL samples from interglacial lacustrine
1004 units (NW11 and THG 4 from Switzerland; Lowick et al., 2012) and found that K-feldspar
1005 amounts only to ~2–4 %. The major component of the samples was quartz (40–50 %).
1006 Tsukamoto et al. (2012) confirmed similar observations for various loess samples using X-ray
1007 diffractometry (XRD) as well as scanning electron microscopy-energy dispersive X-ray (SEM-
1008 EDX). While quartz samples emit RF in the IR region, but not beyond 735 nm (Schmidt et al.,
1009 2015), quartz may not interfere with the main IR-RF emission (865 nm). However, the
1010 polymineral composition may lead to unfortunate emission spectra with, e.g., a dominating peak
1011 at 710 nm (cf. Heydari et al., 2021, for an unsuccessful IR-RF dating attempt using
1012 polyminerals). Hence, for such an application, spectrometer measurements appear indispensable.
1013 Besides, deploying IR-RF on polymineral fine grain samples would significantly broaden the

1014 application to environmental settings where grain sizes $<90 \mu\text{m}$ dominate, and applications can
1015 be tested preferably without extensive methodological research.

1016 In summary, the current status of IR-RF dating still leaves room for rich methodological and
1017 application studies towards a potentially bright future.

1018 **Acknowledgements**

1019 We are grateful to Sébastien Huot, Frank Preusser and two anonymous reviewers for their
1020 patience, constructive comments, and strong support for this manuscript. M.K. Murari and M.
1021 Fuchs were supported by the German Research Foundation (DFG FU417/19-1). S. Kreutzer and
1022 N. Mercier received financial support by the LaScArBx. LaScArBx is a research programme
1023 supported by the ANR (ANR-10-LABX-52). The contribution of S. Kreutzer in 2020 received
1024 funding from the European Union's Horizon 2020 research and innovation programme under the
1025 Marie Skłodowska-Curie grant agreement No 844457 (CREdit). M. Frouin was supported by the
1026 John Fell Fund (161/067 and 171/006) University of Oxford. N. Klasen received funding by the
1027 Deutsche Forschungsgemeinschaft (DFG, German Research Foundation) – Project number
1028 57444011 – CRC 806 "Our way to Europe ". All authors thank L. Diehl for drawing Figure 3.

1029

1030 **Figure captions**

1031 **Figure 1**

1032 Schematic of the different luminescence transitions involved in IR-RF, IRSL and post-IR IRSL
1033 measurements, based on Trautmann et al. (1998, 1999a, 2000a) and Jain and Ankjærgaard
1034 (2011). Colours read as follows: Black lines indicate electron transitions; blue lines indicate hole
1035 migrations. Red colours also refer to electron transitions but related to the production of IRSL.
1036 [a] Exposure to ionizing radiation results in a constant flux of electrons from the valence band to
1037 the conduction band. These electrons may recombine radiatively [b], non-radiatively (not-shown
1038 for clarity), drop immediately back to the valence band (not-shown for clarity) or populate the
1039 IRSL trap [c]. Electrons that populate the IRSL trap pass through the excited state, resulting in
1040 infrared radiofluorescence (1.43 eV). Electrons within the IRSL trap are sensitive to infrared
1041 light and preferentially recombine with proximal holes. Additionally, the electrons may tunnel
1042 directly from the ground-state of the trap [d] (anomalous fading). Alternatively, Trautmann
1043 (2000) and Trautmann et al. (2000a) proposed hole production by allowing a direct transition of
1044 electrons into the valence band. This facilitates new possibilities for the recombination of
1045 electrons in the IRSL trap [e]. Note that each electron stimulated from the valence band will
1046 result in the production of a hole. However, these are not shown for clarity. If the electrons are
1047 stimulated with infrared light, they reach the excited state of the trap, from which they can
1048 migrate locally [f] before recombining. Higher temperature stimulations provide phonon-
1049 assistance (dashed black arrows), allowing post-IR IRSL signals to be measured from electrons
1050 that have diffused through the band-tail states to more distal holes [g], which are thermally and
1051 athermally more stable.

1052 **Figure 2**

1053 Schematic representation of self-made and commercially available measurement devices. A) The
1054 device used by Erfurt (redrawn after Erfurt et al., 2003). B) The device used by Schilles (redrawn
1055 after Schilles, 2002). C) The device manufactured by Risø laboratories (redrawn after Lapp et al.,
1056 2012). D) The device manufactured by Freiberg Instruments (redrawn after Richter et al., 2013)

1057

1058 **Figure 3**

1059 The efficiencies of four different spectrometers. The overall efficiencies of spectrometers were
1060 approximated by multiplying the individual efficiencies of the grating with those of the
1061 spectrograph and the CCD chip.

1062 **Figure 4**

1063 Effective detection band for (A) the setups used by Schilles (2002) and Erfurt (2003b), and (B)
1064 *Risø* and *lexsyg research* readers. The net transitions were estimated by interpolation and by
1065 multiplying the filter transmission and quantum efficiency of the PMT.

1066 **Figure 5**

1067 Simulated Gaussian IR-RF peaks from K-feldspar at 710 nm, 865 nm and 910 nm (similar to
1068 Erfurt and Krbetschek, 2003b). The main IR-RF peak is centred at 865 nm. A) Simulated IR-RF
1069 spectrum with a high 865 nm peak, simulating a bleached sample. B) Simulated IR-RF spectrum
1070 with a high 710 nm peak, a situation appearing when the sample is dosed. C) A typical spectrum
1071 from K-feldspar for a sediment sample (redrawn after Schilles, 2002).

1072 **Figure 6**

1073 IR-RF bleaching using different bleaching sources. A) Sunlight bleaching (redrawn after
1074 Trautmann et al., 1999a). Full signal resetting is reached within 4–6 h. B) Monochromatic
1075 bleaching for wavelengths <500 nm; a bleaching plateau seems to be reached within ca. 0.3 h
1076 (redrawn after Trautmann et al., 2000a). C) Solar simulator (200 W high-pressure Hg-lamp, 5
1077 mm Schott KG3 heat absorbing filter at a distance 20 cm) allows full signal resetting within 0.7 h
1078 (redrawn after Krbetschek et al., 2000). D) A bleaching comparison of IR-RF measured at
1079 elevated temperature (RF₇₀) with IR₅₀, pIRIR₂₂₅ and pIRIR₂₉₀ (redrawn after Frouin et al., 2017).
1080 Resetting of the IR-RF signal is much slower compared to IR₅₀ and pIRIR₂₂₅, but it is similar or
1081 slightly faster than pIRIR₂₉₀ and needs ~3 h bleaching time. The x-axis scale is similar for all
1082 subplots.

1083 **Figure 7**

1084 IR phosphorescence of a K-feldspar sample after bleaching as observed by Erfurt and
1085 Krbetschek (2003b) (redrawn after Erfurt and Krbetschek, 2003b).

1086 **Figure 8**

1087 A schematic representation to explain the sensitivity change monitored by various authors using
1088 different methods. A) Derived sensitivity correction factor (s) by fitting exponential functions to
1089 two bleached regenerated IR-RF (RF_{reg}) curves (Schilles, 2002). B) Sensitivity correction factor
1090 (F_s) estimation using spline fitting and extrapolation (Varma et al., 2013). C) Sensitivity
1091 correction of IR-RF data by sliding the natural IR-RF (RF_{nat}) curve vertically up or down along
1092 with horizontal sliding to find the best match with the RF_{reg} curve (see main text for detail).

1093 **Figure 9**

1094 A) A typical behaviour of the initial rise of IR-RF from a natural sample. The first few channels
1095 of the measured data show an initial rise in IR-RF intensity before decaying monotonically. B)
1096 IR-RF signal dynamic range measured while irradiating the sample with a cumulative dose of
1097 3,900 Gy. The typical dynamic range of IR-RF signals is ~ 2 , as reported by Schilles (2002) and
1098 (Erfurt, 2003b).

1099 **Figure 10**

1100 IR-RF signal stability with respect to pulse annealing temperature. A) All natural IR-RF (RF_{nat})
1101 signals measured for a fixed short duration at different annealing temperatures. All samples show
1102 an increase in IR-RF up to 150 °C. For samples Gro8 and Es1 the signal decrease for
1103 temperatures > 250 °C, but remains stable for sample Ook1, a >1 Ma old sample (redrawn after
1104 Trautmann et al., 1999a). B) The signal remains stable until ca 250 °C for RF_{nat} and regenerated
1105 IR-RF (RF_{reg}) for sample TH8 and changes its intensity for temperatures >250 °C (redrawn after
1106 Frouin et al., 2017).

1107 **Figure 11**

1108 Graphical representation of IR-RF data analysis techniques used to determine the D_e . A) The D_e
1109 is obtained by extrapolation using the fitted natural IR-RF signal. B) The natural IR-RF signal is

1110 used to re-calculate the D_e using the fitted regenerated IR-RF curve after bleaching. C) The
1111 natural and the regenerated IR-RF signals are recorded before both are matched via (horizontal)
1112 sliding. D) The natural curve is moved up or down via vertically sliding to find both curves' best
1113 match. The D_e is defined as the offset of the natural signal on the x-axis (for further details, see
1114 main text).

1115 **Figure 12**

1116 Simulated IR-RF curves for different equations reported in the literature, with Φ_0 the initial IR-
1117 RF photon flux, $\Delta\Phi$ the dose-dependent change of the IR-RF flux, λ the decay parameter, β the
1118 dispersion factor and D the dose. For similar parameter values, the curve shapes differ markedly.
1119 Values chosen for the figure: $\Phi_0 = 1$, $\Delta\Phi = 1$, $\lambda = 2.274\text{e-}03$, $\beta = 7.6\text{e-}01$.

1120 **Figure 13**

1121 A) Independent age control vs IR-RF age (redrawn after Degering and Krbetschek, 2007). All
1122 IR-RF ages match within the error limits when compared to independent ages. B) All IR-RF ages
1123 show either over or underestimation compared to independent age control (redrawn from
1124 supplement data, Buylaert et al., 2012). C) Independent age control vs IR-RF ages measured with
1125 a modified IRSAR protocol (RF₇₀) (redrawn after Frouin et al., 2017). Almost all ages match
1126 within 2σ uncertainty. Abbreviations used in figure legends: IR-RF SOL2: IR-RF ages when
1127 samples are bleached for 4 h using the external solar lamp Hönle SOL2, Biost.: Biostratigraphy,
1128 IRSL-50_{fc}: Fading corrected IRSL age.

1129

Table captions

Table 1: The main emission bands and possible defects observed in feldspar (copyright by Prasad 2017, permission granted by the author).

Table 2: Irradiation source parameters for various devices used for IR-RF stimulation.

Table 3: The relevant parameters for different spectrometer configurations.

Table 4: Detection parameters for various devices used for IR-RF detection.

Table 5: Bleaching source parameters for various devices used for IR-RF bleaching.

Table 6: Overview of published IR-RF measurement protocols used for D_e determination.

Table 1:

<i>Emission band</i>	<i>Excitation</i>	<i>Possible origin</i>	<i>Reference</i>
~3.8–4.4 eV (280–320 nm)	TL	Strain and/or ionic diffusion	Garcia-Guinea et al. (1999)
	PL	Tl ⁺	Gorobets et al. (1995)
	IRSL		Baril and Huntley (2003a)
	TR-OSL		Clark and Bailiff (1998)
~3.1 eV (400 nm)	CL	Paramagnetic defect	*Finch and Klein (1999)
	IRSL	?	Rieser et al. (1999)
	IRSL	?	Baril and Huntley (2003a)
~2.2 eV (560 nm)	IRSL	Mn ²⁺	Rieser et al. (1997)
	IRSL		Baril and Huntley (2003a)
	CL		Geake et al. (1977)
	TR-OSL		Clark and Bailiff (1998)
~1.7 eV (730 nm)	Absorption	Fe ³⁺	White et al. (1986)
	PL		Telfer and Walker (1975)
	IRSL		Krbetschek et al. (1997)
	PL		Poolton et al. (1996, 2006)
~1.45 eV (855 nm)	RL or RF	IRSL dating trap	Trautmann et al. (1998)
~1.41–1.3 eV (900 nm) (~880 nm and ~955 nm)	CL (at 7 K)	IRCL trap with two sites and Fe ⁴⁺ as a competitor	Kumar et al. (2020)
~1.3–1.36 eV (910 nm)	RL or RF	Pb ⁺	Erfurt (2003b)
	Post IR phosphorescence	IRSL dating trap	Baril and Huntley (2003a)
	TL	?	Krbetschek and Rieser (1995)

TL: Thermoluminescence, IRSL: Infrared stimulated luminescence, CL: Cathodoluminescence, RF: Radiofluorescence, RL: Radioluminescence, PL: Photoluminescence

TR-OSL: Time-resolved optically stimulated luminescence, IRCL: Infrared Cathodoluminescence

* Finch and Klein (1999) reported the peak maximum at 430 nm related to Al³⁺-O²⁻-Al³⁺ “Löwenstein” bridges.

Table 2:

<i>Laboratory / Manufacturer</i>	<i>Radiation source</i>	<i>Activity [GBq]</i>	<i>Radiation Type</i>	<i>Source type</i>	<i>Dose rate [Gy min⁻¹]</i>	<i>Active area [mm²]</i>	<i>Reference</i>
Freiberg	¹³⁷ Cs/ ¹³⁷ Ba	0.0037	β and γ	Planar	0.050	19.6	Trautmann (1999)
Freiberg	¹³⁷ Cs/ ¹³⁷ Ba	0.0050	β and γ	Planar	0.080	50.3	Erfurt (2003b)
Heidelberg	¹³⁷ Cs/ ¹³⁷ Ba	0.0037	β and γ	Planar	0.034	28.3	Schilles (2002)
Risø	⁹⁰ Sr/ ⁹⁰ Y	1.48	β	Planar	2.640	50.3	Buylaert et al. (2012)
Freiberg Instruments	⁹⁰ Sr/ ⁹⁰ Y	1.6–2	β	Ring	2.250	n.a.	Richter et al. (2012)

Erfurt calibrated the radiation source with Al₂O₃:C while the other readers were calibrated with natural (calibration) quartz.

Table 3:

<i>Laboratory / Manufacturer</i>	Spectrograph	<i>Spectrograph/Grating</i>		Dispersion [nm]	Company	<i>CCD Camera</i>			<i>Reference</i>
		Grating	Blazed			Camera type	Active Pixels	Cooling Type	
Freiberg	Jobin Yvon CP200	Holographic	Not applicable	300–1000	Marconi	NA	1152x298	-100 °C (Liquid nitrogen)	Rieser et al. (1994)
Freiberg	Jobin-Yvon CP200	Holographic	Not applicable	250–1152	Marconi	Front-illuminated	1152x352	-100 °C (Liquid nitrogen)	Erfurt (2003b), Rieser et al. (1994)
Heidelberg	Acton SP150	150 lines/mm	300 nm	200–1100	Princeton Instruments	Back-illuminated	1100x330	-100 °C (Liquid nitrogen)	Rieser et al. (1999)
Freiberg Instruments	Andor Shamrock 163	300 lines/mm	500 nm	200–1050	Andor Newton 920-BU/iDus 420 OE	Back-illuminated / Open Electrode	1024x255	-80 °C (TE Cooled)	Richter et al. (2013)

TE Cooled: Thermoelectric cooling

Table 4:

<i>Laboratory/ Manufacturer</i>	<i>Detector</i>	<i>Detection [nm]</i>	<i>Filters</i>	<i>Bandpass [nm]</i>	<i>Light collection</i>	<i>References</i>
Freiberg	Spectrometer	300–1000	No filter	300-1000	Optical Guide	*Trautmann (1999)
Freiberg	Spectrometer / Hamamatsu (R943-02)	160–930	HQ865/20	855-875	Optical Guide	#Erfurt (2003b)
Heidelberg	Spectrometer / Hamamatsu (R943-02)	160–930	IR83 HOYA	820-930	Optical Guide	#Schilles (2002)
Risø	Hamamatsu (H7421-50)	380–890	Chroma D900/100	850-890	Optical Guide	Buylaert et al. (2012)
Freiberg Instruments	Spectrometer / Hamamatsu (H7421-50)	380–890	Chroma D850/40	845-885	Direct	Richter et al. (2013)

*Trautmann's research was based on spectrometer measurements using a 200–800 nm detection range. Later, the spectrometer was modified for detecting 300–1,000 nm. The integrated counts of IR-RF peak were used to estimate the D_e .

#Schilles and Erfurt used liquid-cooled thermoelectric housing (LCT50, Thorn EMI) at about $-20\text{ }^{\circ}\text{C}$ to reduce the thermal noise.

Table 5:

<i>Laboratory/ Manufacturer</i>	<i>Bleaching source</i>	<i>Spectrum</i>	<i>Max Power*</i> <i>[mW cm⁻²]</i>	<i>Connection</i>	<i>Reference</i>
Freiberg	Hg-Lamp	UV-VIS	--	Optical Guide	# Trautmann (1999)
Freiberg	250W OSRAM LAMP	UV-VIS	100	Optical Guide	*Erfurt (2003b)
Heidelberg	150W QTH	UV-VIS	80	Optical Guide	*Schilles (2002)
Risø	UV LED	UV	700	Direct	Buylaert et al. (2012)
Freiberg Instruments	6 LED solar simulator	UV-IR	700	Direct	Richter et al. (2013)

*Maximum power density of the bleaching units refers to approximate power at the sample position. It can vary from device to device.

#Trautmann (1999) used an interference filter in front of the solar lamp for monochromatic bleaching.

*Schilles (2002) and Erfurt (2003b) both used an IR cut-off filter.

1 Table 6:

Reference	Protocol Abbr.	Treatments and observations ¹						Data analysis	Comments
		#1	#2	#3	#4	#5	#6		
Buylaert et al. (2012)	NA (based on IRSAR)	-	IR-RF [RF_{nat}]	Bleaching ($\geq 1,800$ s) (ca. 395 nm)	Pause ($\geq 3,600$ s)	-	IR-RF [RF_{reg}]	Sliding	-
Erfurt and Krbetschek (2003b)	IRSAR	-	IR-RF [RF_{nat}]	Bleaching ($\geq 1,800$ s) (artificial solar spectrum)	Pause ($\geq 3,600$ s)	-	IR-RF [RF_{reg}]	Fitting (interp.)	RF_{nat} is represented by only a few channels
Frouin et al. (2017)	RF ₇₀ (based on IRSAR)	PH@70 °C (900 s)	IR-RF@70 °C [RF_{nat}]	Bleaching@70 °C ($\geq 7,200$ s) (artificial solar spectrum)	Pause ($\geq 3,600$ s)	PH@70 °C (900 s)	IR-RF@70 °C [RF_{reg}]	Sliding	-
Krbetschek et al. (2000)	NA	-	IR-RF [RF_{nat}]	Bleaching ($\geq 1,800$ s) (artificial solar spectrum)	-	-	IR-RF [RF_{reg}]	Fitting Sliding	Based on the results by Trautmann et al. (1999a), but with artificial bleaching
Trautmann et al. (1999a)	NA	-	IR-RF [RF_{nat}]	Bleaching (natural sunlight)	-	-	IR-RF [RF_{reg}]	Fitting (extrapol.)	RF_{reg} is represented by only a few channels
Schilles (2002)	NA	-	IR-RF [RF_{nat}]	Bleaching $\geq 3,600$ s) (artificial solar spectrum)	Pause ($\geq 1,800$ s)	-	IR-RF [RF_{reg}]	Fitting	Combination of extrapolation and interpolation for the data analysis; sensitivity correction using a separate aliquot (Schilles, 2002, p. 97)
Varma et al. (2013) ²	NA (based on IRSAR)	-	IR-RF [RF_{nat}]	Bleaching (≥ 800 s) (ca. 395 nm)	-	-	IR-RF [RF_{reg}]	Sliding	200 s phosphorescence measurement before and after each IR-RF measurement; Repeat step #3 and #6 to monitor sensitivity changes

2 ¹The instrumental setup differs considerably across the studies and should be considered before protocol application. If no measurement temperature is listed, such value was not
3 reported by the study or no additional heating above ambient temperature was applied. Please note that the table lists only general treatments, for further details the reader is
4 referred to the respective publication.

5 ²The authors used their protocol for dose recovery tests only; distinct D_e determinations are not mentioned.

6 PH: Preheat | NA: Not available

7

8

9 **References**

- 10 Aitken, M.J., 1985a. Thermoluminescence dating. Academic Press.
- 11 Aitken, M.J., 1985b. Alpha particle effectiveness: numerical relationship between systems.
12 Ancient TL 3, 22–25.
- 13 Aitken, M.J., 1998. An introduction to optical dating. Oxford University Press.
- 14 Auclair, M., Lamothe, M., Huot, S., 2003. Measurement of anomalous fading for feldspar IRSL
15 using SAR. Radiation Measurements 37, 487–492. doi:10.1016/S1350-4487(03)00018-0
- 16 ASTM International, 2012. ASTM G173-03(2012) Standard Tables for Reference Solar Spectral
17 Irradiances: Direct Normal and Hemispherical on 37° Tilted Surface, ASTM International,
18 West Conshohocken, PA. <http://www.astm.org>. doi: 10.1520/G0173-03R12
- 19 Baril, M.R., Huntley, D.J., 2003a. Optical excitation spectra of trapped electrons in irradiated
20 feldspars. J. Phys.: Condens. Matter 15, 8011–8027. doi: 10.1088/0953-8984/15/46/017.
- 21 Baril, M.R., Huntley, D.J., 2003b. Infrared stimulated luminescence and phosphorescence
22 spectra of irradiated feldspars. J. Phys.: Condens. Matter 15, 8029–8048. doi: 10.1088/0953-
23 8984/15/46/018.
- 24 Baumann, W., Mania, D., Toepfer, V., Eißmann, L., 1983. Die paläolithischen Neufunde von
25 Markkleeberg bei Leipzig. Landesmuseum für Vorgeschichte Dresden 16.
- 26 Brooks, R.J., Finch, A.A., Hole, D.E., Townsend, P.D., Wu, Z.-L., 2002. The red to near-infrared
27 luminescence in alkali feldspar. Contributions to Mineralogy and Petrology 143, 484–494.
28 doi: 10.1007/s00410-002-0359-4.
- 29 Buylaert, J.P., Jain, M., Murray, A.S., Thomsen, K.J., Lapp, T., 2012. IR-RF dating of sand-
30 sized K-feldspar extracts: A test of accuracy. Radiation Measurements 47, 759–765. doi:
31 10.1016/j.radmeas.2012.06.021.
- 32 Buylaert, J.P., Murray, A.S., Thomsen, K.J., Jain, M., 2009. Testing the potential of an elevated
33 temperature IRSL signal from K-feldspar. Radiation Measurements 44, 560–565. doi:
34 10.1016/j.radmeas.2009.02.007.

- 35 Clark, R.J., Bailiff, I.K., 1998. Fast time-resolved luminescence emission spectroscopy in some
36 feldspars. *Radiation Measurements* 29, 553–560. doi: 10.1016/S1350-4487(98)00068-7.
- 37 Coussot, C., Liard, M., Kreutzer, S., Mercier, N., 2019. Séquence de Comblement d'un
38 Paléovallon en Contexte de Plateau (290-10 Ka) : La Coupe De Courville-Sur-Eure (Eure-
39 Et-Loir, France). *Quaternaire*, 167–183.
- 40 Degering, D., Krbetschek, M.R., 2007. Dating of interglacial sediments by luminescence
41 methods, in: *The climate of past interglacials. Developments in Quaternary Sciences.*
42 Elsevier, pp. 157–171. doi: 10.1016/S1571-0866(07)80036-4.
- 43 Duller, G.A.T., 1992. Luminescence chronology of raised marine terraces, South-West North
44 Island, New Zealand. PhD thesis, University of Aberystwyth, UK, pp. 236.
- 45 Efron, B., 1979. Bootstrap Methods: Another Look at the Jackknife. *Ann. Statist.* 7, 1–26. doi:
46 10.1214/aos/1176344552.
- 47 Eissmann, L., 2002. Quaternary geology of eastern Germany (Saxony, Saxon-Anhalt, South
48 Brandenburg, Thüringia), type area of the Elsterian and Saalian Stages in Europe.
49 *Quaternary Science Reviews* 21, 1275-1346. doi: 10.1016/S0277-3791(01)00075-0.
- 50 Erfurt, G., 2003a. Infrared luminescence of Pb⁺ centres in potassium-rich feldspars. *Physica*
51 *status solidi (a)* 200, 429–438. doi: 10.1002/pssa.200306700.
- 52 Erfurt, G., 2003b. Radiolumineszenzspektroskopie und -dosimetrie an Feldspäten und
53 synthetischen Luminophoren für die geochronometrische Anwendung. PhD thesis,
54 Technische Universität Bergakademie Freiberg, Germany, pp. 141.
- 55 Erfurt, G., Krbetschek, M.R., 2003a. Studies on the physics of the infrared radioluminescence of
56 potassium feldspar and on the methodology of its application to sediment dating. *Radiation*
57 *Measurements* 37, 505–510. doi: 10.1016/S1350-4487(03)00058-1.
- 58 Erfurt, G., Krbetschek, M.R., 2003b. IRSAR - A single-aliquot regenerative-dose dating protocol
59 applied to the infrared radiofluorescence (IR-RF) of coarse-grain K-feldspar. *Ancient TL* 21,
60 35–42.

- 61 Erfurt, G., Krbetschek, M.R., Bortolot, V.J., Preusser, F., 2003. A fully automated multi-spectral
62 radioluminescence reading system for geochronometry and dosimetry. *Nuclear Instruments
63 and Methods in Physics Research Section B: Beam Interactions with Materials and Atoms*
64 207, 487–499. doi: 10.1016/S0168-583X(03)01121-2.
- 65 Finch, A.A., Klein, J., 1999. The causes and petrological significance of cathodoluminescence
66 emissions from alkali feldspars. *Contributions to Mineralogy and Petrology* 135, 234–243.
67 doi: 10.1007/s004100050509.
- 68 Frouin, M., 2014. Les feldspaths comme support pour la datation par luminescence de gisements
69 archéologiques et de séquences quaternaires d’Aquitaine. PhD thesis, Université Bordeaux
70 Montaigne, France, pp. 390.
- 71 Frouin, M., Huot, S., Kreutzer, S., Lahaye, C., Lamothe, M., Philippe, A., Mercier, N., 2017. An
72 improved radiofluorescence single-aliquot regenerative dose protocol for K-feldspars.
73 *Quaternary Geochronology* 38, 13–24. doi: 10.1016/j.quageo.2016.11.004.
- 74 Frouin, M., Huot, S., Mercier, N., Lahaye, C., Lamothe, M., 2015. The issue of laboratory
75 bleaching in the infrared-radiofluorescence dating method. *Radiation Measurements* 81,
76 212–217. doi: 10.1016/j.radmeas.2014.12.012.
- 77 Fu, X., Zhang, J.-F., Zhou, L.-P., 2012. Comparison of the properties of various optically
78 stimulated luminescence signals from potassium feldspar. *Radiation Measurements* 47, 210–
79 218. doi:10.1016/j.radmeas.2011.12.007
- 80 Garcia-Guinea, J., Townsend, P.D., Sanchez-Muñoz, L., Rojo, J.M., 1999. Ultraviolet-blue ionic
81 luminescence of alkali feldspars from bulk and interfaces. *Physics and Chemistry of*
82 *Minerals* 26, 658–667. doi: 10.1007/s002690050231.
- 83 Geake, J.E., Walker, G., Telfer, D.J., Mills, A.A., 1977. The cause and significance of
84 luminescence in lunar plagioclase. *Philosophical Transactions of the Royal Society A:
85 Mathematical, Physical and Engineering Sciences* 285, 403–408. doi:
86 10.1098/rsta.1977.0081.

- 87 Gorobets, B.S., Portnov, A.M., Rogozhin, A.A., 1995. Luminescence spectroscopy of the earth.
88 Radiation Measurements 24, 485–491. doi: 10.1016/1350-4487(94)00124-J.
- 89 Guérin, G., Valladas, G., 1980. Thermoluminescence dating of volcanic plagioclases. Nature
90 286, 697–699. doi: 10.1038/286697a0.
- 91 Herber, L.J., 1969. Separation of Feldspar from Quartz by Flotation. The American Mineralogist
92 54, 1212–1215.
- 93 Hetzel, R., Tao, M., Niedermann, S., Strecker, M.R., Ivy-Ochs, S., Kubik, P.W., Gao, B., 2004.
94 Implications of the fault scaling law for the growth of topography: mountain ranges in the
95 broken foreland of north-east Tibet. Terra Nova 16, 157–162. doi:10.1111/j.1365-
96 3121.2004.00549.x
- 97 Heydari, M., Guérin, G., Zeidi, M., Conard, N. J., 2021. Bayesian luminescence dating at Ghār-e
98 Boof, Iran, provides a new chronology for Middle and Upper Paleolithic in the southern
99 Zagro. Journal of Human Evolution 151, 102926. doi:10.1016/j.jhevol.2020.102926
- 100 Huntley, D.J., 2006. An explanation of the power-law decay of luminescence. J. Phys.: Condens.
101 Matter 18, 1359–1365. doi: 10.1088/0953-8984/18/4/020.
- 102 Huntley, D.J., Godfrey-Smith, D., Thewalt, M., 1985. Optical dating of sediments. Nature 14,
103 27-33. <https://doi.org/10.1038/313105a0>.
- 104 Huntley, D.J., Lamothe, M., 2001. Ubiquity of anomalous fading in K-feldspars and the
105 measurement and correction for it in optical dating. Canadian Journal of Earth Sciences 38,
106 1093–1106. doi: 10.1139/cjes-38-7-1093.
- 107 Huntley, D.J., Lian, O.B., 2006. Some observations on tunnelling of trapped electrons in
108 feldspars and their implications for optical dating. Quaternary Science Reviews 25, 2503–
109 2512. doi: 10.1016/j.quascirev.2005.05.011.
- 110 Hütt, G., Jaek, I., Tchonka, J., 1988. Optical dating: K-Feldspars optical response stimulation
111 spectra. Quaternary Science Reviews 7, 381–385. doi: 10.1016/0277-3791(88)90033-9.

- 112 Huot, S., Frouin, M., Lamothe, M., 2015. Evidence of shallow TL peak contributions in infrared
113 radiofluorescence. *Radiation Measurements* 81, 237–241. doi:
114 10.1016/j.radmeas.2015.05.009.
- 115 Jain, M., Ankjærgaard, C., 2011. Towards a non-fading signal in feldspar: Insight into charge
116 transport and tunnelling from time-resolved optically stimulated luminescence. *Radiation*
117 *Measurements* 46, 292–309. doi: 10.1016/j.radmeas.2010.12.004.
- 118 Kadereit, A., Kühn, P., Wagner, G.A., 2010. Holocene relief and soil changes in loess-covered
119 areas of south-western Germany: The pedosedimentary archives of Bretten-Bauerbach
120 (Kraichgau). *Quaternary International* 222, 96–119. doi: 10.1016/j.quaint.2009.06.025.
- 121 Kars, R.H., Wallinga, J., 2009. IRSL dating of K-feldspars: Modelling natural dose response
122 curves to deal with anomalous fading and trap competition. *Radiation Measurements* 44,
123 594–599.
- 124 Klasens, H.A., 1946. Transfer of energy between centres in zinc sulphide phosphors. *Nature* 158,
125 306–307. doi: 10.1038/158306c0.
- 126 Krbetschek, M.R., Götze, J., Irmer, G., Rieser, U., Trautmann, T., 2002. The red luminescence
127 emission of feldspar and its wavelength dependence on K, Na, Ca \pm composition.
128 *Mineralogy and Petrology* 76, 167–177. doi:10.1007/s007100200039
- 129 Krbetschek, M.R., Degering, D., Alexowsky, W., 2008. Infrarot-Radiofluoreszenz-Alter (IR-RF)
130 unter-saalezeitlicher Sedimente Mittel- und Ostdeutschlands. *Zeitschrift der Deutschen*
131 *Gesellschaft für Geowissenschaften* 159, 133–140. doi: 10.1127/1860-1804/2008/0159-
132 0133.
- 133 Krbetschek, M.R., Götze, J.U., Dietrich, A., Trautmann, T., 1997. Spectral information from
134 minerals relevant for luminescence dating. *Radiation Measurements* 27, 695–748. doi:
135 10.1016/S1350-4487(97)00223-0.
- 136 Krbetschek, M.R., Rieser, U., 1995. Luminescence spectra of alkali feldspars and plagioclases.
137 *Radiation Measurements* 24, 473–477. doi: 10.1016/1350-4487(95)00011-3.

- 138 Krbetschek, M.R., Trautmann, T., 2000. A spectral radioluminescence study for dating and
139 dosimetry. *Radiation Measurements* 32, 853–857. doi: 10.1016/S1350-4487(00)00085-8.
- 140 Krbetschek, M.R., Trautmann, T., Dietrich, A., Stolz, W., 2000. Radioluminescence dating of
141 sediments: methodological aspects. *Radiation Measurements* 32, 493–498. doi:
142 10.1016/S1350-4487(00)00122-0.
- 143 Krbetschek, M.R., Erfurt, G., Degering, D. 2003. *Radiofluorescence dating: A novel method for*
144 *age determination of clastic sediment deposits from about 20 ka to 300 ka.* Poster
145 presentation; XVI Inqua Congress, Reno (USA).
- 146 Kreutzer, S., Duval, M., Bartz, M., Bertran, P., Bosq, M., Eynaud, F., Verdin, F., Mercier, N.,
147 2018a. Deciphering long-term coastal dynamics using IR-RF and ESR dating: A case study
148 from Médoc, south-west France. *Quaternary Geochronology* 48, 108–120. doi:
149 10.1016/j.quageo.2018.09.005.
- 150 Kreutzer, S., Lauer, T., Meszner, S., Krbetschek, M.R., Faust, D., Fuchs, M., 2014. Chronology
151 of the Quaternary profile Zeuchfeld in Saxony-Anhalt / Germany – a preliminary
152 luminescence dating study. *Zeitschrift für Geomorphologie* 58, 5–26. doi: 10.1127/0372-
153 8854/2012/S-00112.
- 154 Kreutzer, S., Martin, L., Dubernet, S., Mercier, N., 2018b. The IR-RF alpha-Efficiency of K-
155 feldspar. *Radiation Measurements* 120, 148–156. doi: 10.1016/j.radmeas.2018.04.019.
- 156 Kreutzer, S., Burow, C., Dietze, M., Fuchs, M., Schmidt, C., Fischer, M., Friedrich, J., 2018c.
157 Luminescence: Comprehensive Luminescence Dating Data Analysis. R package version
158 0.8.6, <https://CRAN.R-project.org/package=Luminescence>.
- 159 Kreutzer, S., Murari, M.K., Frouin, M., Fuchs, M., Mercier, N., 2017. Always remain suspicious:
160 a case study on tracking down a technical artefact while measuring IR-RF. *Ancient TL* 35,
161 20–30.
- 162 Kreutzer, S., Schmidt, C., Fuchs, M.C., Dietze, M., Fischer, M., Fuchs, M., 2012. Introducing an
163 R package for luminescence dating analysis. *Ancient TL* 30, 1–8.

- 164 Kumar, R., Kook, M., Murray, A.S., Jain, M., 2018. Towards direct measurement of electrons in
165 metastable states in K-feldspar: Do infrared-photoluminescence and radioluminescence
166 probe the same trap? *Radiation Measurements* 120, 1–17. doi:
167 10.1016/j.radmeas.2018.06.018.
- 168 Kumar, R., Martin, L.I.D.J., Poelman, D., Vandenberghe, D., De Grave, J., Kook, M., Jain, M.,
169 2020. Site-selective mapping of metastable states using electron-beam induced luminescence
170 microscopy. *Sci Rep* 10, 1270–14. doi:10.1038/s41598-020-72334-7
- 171 Kumar, R., Kook, M., Jain, M., 2021. Sediment dating using Infrared Photoluminescence.
172 *Quaternary Geochronology* 62, 101147. doi:10.1016/j.quageo.2020.101147
- 173 Lamothe, M., Auclair, M., Hamzaoui, C., Huot, S., 2003. Towards a prediction of long-term
174 anomalous fading of feldspar IRSL. *Radiation Measurements* 37, 493–498.
- 175 Lamothe, M., Brisson, L.F., Hardy, F., 2020. Circumvention of anomalous fading in feldspar
176 luminescence dating using Post-Isothermal IRSL. *Quaternary Geochronology* 57, 101062.
177 doi:10.1016/j.quageo.2020.101062
- 178 Larsen, E., Johannessen, N.E., Kowalczyk, P.B., Kleiv, R.A., 2019. Selective flotation of K-
179 feldspar from Na-feldspar in alkaline environment. *Minerals Engineering* 142, 105928.
180 doi:10.1016/j.mineng.2019.105928
- 181 Lapp, T., Jain, M., Thomsen, K.J., Murray, A.S., Buylaert, J.P., 2012. New luminescence
182 measurement facilities in retrospective dosimetry. *Radiation Measurements* 47, 803–808.
183 doi: 10.1016/j.radmeas.2012.02.006
- 184 Lauer, T., Krbetschek, M.R., Frechen, M., Tsukamoto, S., Hoselmann, C., Weidenfeller, M.,
185 2011. Infrared radiofluorescence (IR-RF) dating of middle pleistocene fluvial archives of the
186 Heidelberg Basin (Southwest Germany). *Geochronometria* 38, 23–33. doi: 10.2478/s13386-
187 011-0006-9.

- 188 Lauer, T., Weiss, M., 2018. Timing of the Saalian- and Elsterian glacial cycles and the
189 implications for Middle – Pleistocene hominin presence in central Europe. *Scientific*
190 *Reports*, 8: 5111. <https://doi.org/10.1038/s41598-018-23541-w>.
- 191 Li, Y., Tsukamoto, S., Frechen, M., Gabriel, G., 2017. Timing of fluvial sedimentation in the
192 Upper Rhine Graben since the Middle Pleistocene: constraints from quartz and feldspar
193 luminescence dating. *Boreas* 47, 256–270. doi:10.1111/bor.12266
- 194 Li, B., Roberts, R.G., Jacobs, Z., Li, S.-H., 2014. A single-aliquot luminescence dating procedure
195 for K-feldspar based on the dose-dependent MET-pIRIR signal sensitivity. *Quaternary*
196 *Geochronology* 20, 51–64. doi:10.1016/j.quageo.2013.11.001
- 197 Li, B., Li, S.-H., 2013. The effect of band-tail states on the thermal stability of the infrared
198 stimulated luminescence from K-feldspar. *Journal of Luminescence* 136, 5–10. doi:
199 10.1016/j.jlumin.2012.08.043.
- 200 Li, B., Li, S.-H., 2011a. Luminescence dating of K-feldspar from sediments: A protocol without
201 anomalous fading correction. *Quaternary Geochronology* 6, 468–479. doi:
202 10.1016/j.quageo.2011.05.001.
- 203 Li, B., Li, S.-H., 2011b. Thermal stability of infrared stimulated luminescence of sedimentary K-
204 feldspar. *Radiation Measurements* 46, 29–36. doi:10.1016/j.radmeas.2010.10.002
- 205 Liu, J., Murray, A.S., Buylaert, J.-P., Jain, M., Chen, J., Lu, Y., 2016. Stability of fine-grained
206 TT-OSL and post-IR IRSL signals from a c. 1 Ma sequence of aeolian and lacustrine
207 deposits from the Nihewan Basin (northern China). *Boreas* 45, 703–714.
208 doi:10.1111/bor.12180
- 209 Lowick, S.E., Trauerstein, M., Preusser, F., 2012. Testing the application of post IR-IRSL dating
210 to fine grain waterlain sediments. *Quaternary Geochronology* 8, 33-40. doi:
211 10.1016/j.quageo.2011.12.003.

- 212 Lowick, S.E., Valla, P.G., 2018. Characterising the luminescence behaviour of 'infinitely old'
213 quartz samples from Switzerland. *Quaternary Geochronology* 43, 1–11. doi:
214 10.1016/j.quageo.2017.09.004.
- 215 Marfunin, A.S., Bershov, L.V., 1970. Paramagnetic in feldspars and their possible
216 crystalchemical and petrological significance (ПАРАМАГНИТНЫЕ ЦЕНТРЫ В
217 ПОЛЕВЫХ ШПАТАХ И ИХ ВОЗМОЖНОЕ КРИСТАЛЛОХИМИЧЕСКОЕ
218 И ПЕТРОГРАФИЧЕСКОЕ ЗНАЧЕНИЕ). *Dokl. Akad. Nauk* 193, 421–414.
- 219 Marfunin, A.S., 1979. *Spectroscopy, luminescence and radiation centers in minerals*. Springer
220 Berlin Heidelberg. doi: 10.1007/978-3-642-67112-8.
- 221 Meszner, S., Kreutzer, S., Fuchs, M., Faust, D., 2013. Late Pleistocene landscape dynamics in
222 Saxony, Germany: Paleoenvironmental reconstruction using loess-paleosol sequences.
223 *Quaternary International* 296, 95–107. doi: 10.1016/j.quaint.2012.12.040.
- 224 Meyer, M.C., Austin, P., Tropper, P., 2013. Quantitative evaluation of mineral grains using
225 automated SEM–EDS analysis and its application potential in optically stimulated
226 luminescence dating. *Radiation Measurements* 58, 1–11. doi:
227 10.1016/j.radmeas.2013.07.004.
- 228 Miallier, D., Sanzelle, S., Fain, J., 1983. The use of flotation technique to separate quartz from
229 feldspar. *Ancient TL* 5–6.
- 230 Mittelstrass, D., Kreutzer, S., preprint. Spatially Resolved Infrared Radiofluorescence: Single-
231 grain K-feldspar Dating using CCD Imaging, *Geochronology Discussion*, 1-31. doi:
232 10.5194/gchron-2020-43
- 233 Murari, M.K., Kreutzer, S., Fuchs, M., 2018. Further investigations on IR-RF: Dose recovery
234 and correction. *Radiation Measurements* 120, 110–119. doi: 10.1016/j.radmeas.2018.04.017.
- 235 Murray, A.S., Buylaert, J.P., Thomsen, K.J., Jain, M., 2009. The effect of preheating on the
236 IRSL signal from feldspar. *Radiation Measurements* 44, 554–559. doi:
237 10.1016/j.radmeas.2009.02.004.

- 238 Murray, A.S., Wintle, A.G., 2000. Luminescence dating of quartz using an improved single-
239 aliquot regenerative-dose protocol. *Radiation Measurements* 32, 57–73. doi: 10.1016/S1350-
240 4487(99)00253-X.
- 241 Nagli, L.E., Dyachenko, S.V., 1988. Influence of a v_c -vacancy on luminescence of Pb^+ centres in
242 alkali halides. *Phys. stat. sol. (b)* 146, 295–301. doi: 10.1002/pssb.2221460131.
- 243 Novothny, Á., Frechen, M., Horváth, E., Krbetschek, M.R., Tsukamoto, S., 2010. Infrared
244 stimulated luminescence and radiofluorescence dating of aeolian sediments from Hungary.
245 *Quaternary Geochronology* 5, 114–119. doi: 10.1016/j.quageo.2009.05.002.
- 246 Ostrooumov, M., 2016. *Amazonite*. Elsevier. doi: 10.1016/C2015-0-00152-6.
- 247 Pavesi, L., Ceschini, M., 1993. Stretched-exponential decay of the luminescence in porous
248 silicon. *Physical Review B* 48, 17625–17628. doi: 10.1103/PhysRevB.48.17625.
- 249 Pagonis, V., Phan, H., Ruth, D., Kitis, G., 2013. Further investigations of tunneling
250 recombination processes in random distributions of defects. *Radiation Measurements* 58, 66–
251 74. doi:10.1016/j.radmeas.2013.08.006
- 252 Pagonis, V., Kulp, C., 2017. Monte Carlo simulations of tunneling phenomena and nearest
253 neighbor hopping mechanism in feldspars. *Journal of Luminescence* 181, 114–120.
254 doi:10.1016/j.jlumin.2016.09.014
- 255 Pagonis, V., Friedrich, J., Discher, M., Müller-Kirschbaum, A., Schlosser, V., Kreutzer, S.,
256 Chen, R., Schmidt, C., 2019. Excited state luminescence signals from a random distribution
257 of defects: A new Monte Carlo simulation approach for feldspar. *Journal of Luminescence*
258 207, 266–272. doi:10.1016/j.jlumin.2018.11.024
- 259 Poolton, N.R.J., Bøtter-Jensen, L., Johnsen, O., 1996. On the relationship between luminescence
260 excitation spectra and feldspar mineralogy. *Radiation Measurements* 26, 93–101. doi:
261 10.1016/1350-4487(95)00288-X.

- 262 Poolton, N.R.J., Bøtter-Jensen, L., Johnsen, O., 1995. Thermo-optical properties of optically
263 stimulated luminescence in feldspars. *Radiation Measurements* 24, 531–534. doi:
264 10.1016/1350-4487(94)00114-G.
- 265 Poolton, N.R.J., Kars, R.H., Wallinga, J., Bos, A.J.J., 2009. Direct evidence for the participation
266 of band-tails and excited-state tunnelling in the luminescence of irradiated feldspars. *J.*
267 *Phys.: Condens. Matter* 21, 485505. doi: 10.1088/0953-8984/21/48/485505.
- 268 Poolton, N.R.J., Mauz, B., Lang, A., Jain, M., Malins, A.E.R., 2006. Optical excitation processes
269 in the near band-edge region of and feldspar. *Radiation Measurements* 41, 542–548. doi:
270 10.1016/j.radmeas.2005.12.001.
- 271 Poolton, N.R.J., Ozanyan, K.B., Wallinga, J., Murray, A.S., Bøtter-Jensen, L., 2002a. Electrons
272 in feldspar II: a consideration of the influence of conduction band-tail states on luminescence
273 processes. *Physics and Chemistry of Minerals* 29, 217–225. doi: 10.1007/s00269-001-0218-
274 2.
- 275 Poolton, N.R.J., Wallinga, J., Murray, A.S., Bulur, E., Bøtter-Jensen, L., 2002b. Electrons in
276 feldspar I: on the wavefunction of electrons trapped at simple lattice defects. *Physics and*
277 *Chemistry of Minerals* 29, 210–216. doi: 10.1007/s00269-001-0217-3.
- 278 Porat, N., Faerstein, G., Medialdea, A., Murray, A.S., 2015. Re-examination of common
279 extraction and purification methods of quartz and feldspar for luminescence dating. *Ancient*
280 *TL* 33, 22–30.
- 281 Prasad, A.K., 2017. Understanding defect related luminescence processes in wide bandgap
282 materials using low temperature multi-spectroscopic techniques. PhD thesis, DTU Nutech,
283 Denmark, pp. 196.
- 284 Prasad, A.K., Jain, M., 2018. Dynamics of the deep red Fe 3+ photoluminescence emission in
285 feldspar. *Journal of Luminescence* 196, 462–469. doi: 10.1016/j.jlumin.2017.11.051.

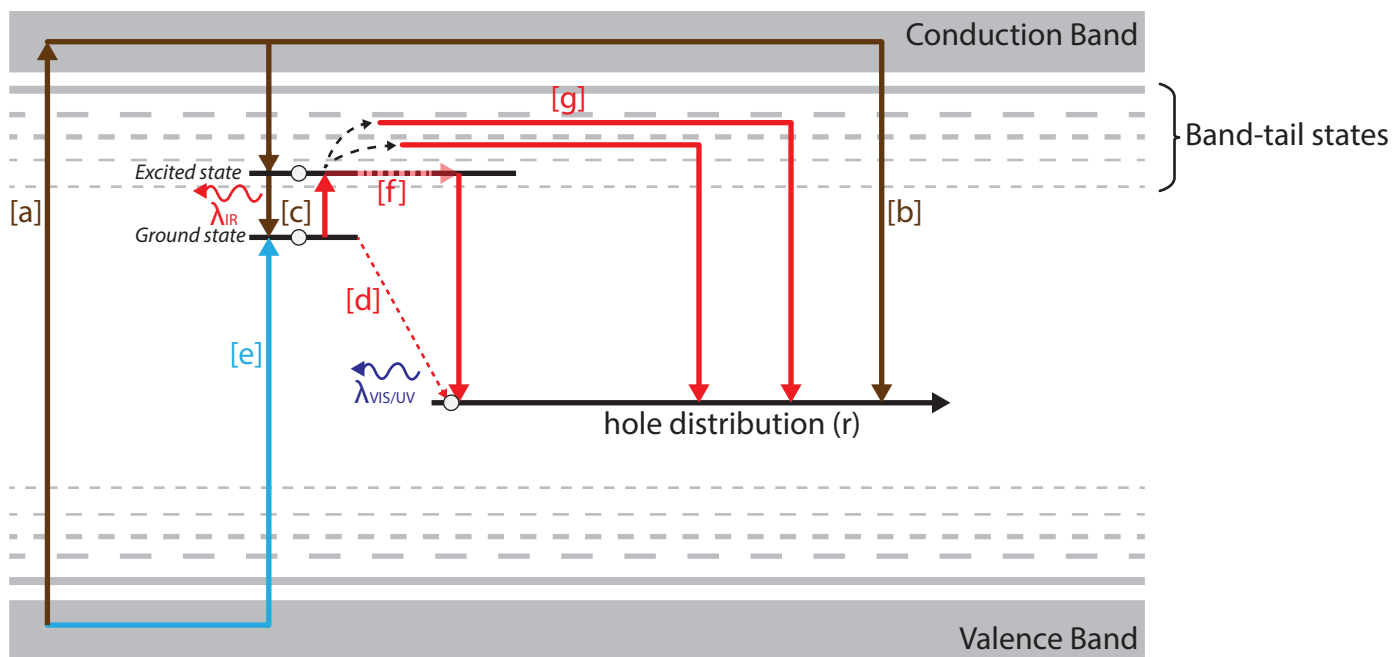
- 286 Prasad, A.K., Poolton, N.R.J., Kook, M., Jain, M., 2017. Optical dating in a new light: A direct,
287 non-destructive probe of trapped electrons. *Sci Rep* 7, 461. doi: 10.1038/s41598-017-10174-
288 8.
- 289 Preusser, F., Degering, D., Fuchs, M., Hilgers, A., Kadereit, A., Klasen, N., Krbetschek, M.R.,
290 Richter, D., Spencer, J.Q.G., 2008. Luminescence dating: basics, methods and applications.
291 *Eiszeitalter und Gegenwart (Quaternary Science Journal)* 57, 95–149. doi: 10.3285/eg.57.1-
292 2.5.
- 293 Prescott, J.R., Huntley, D.J., Hutton, J.T., 1993. Estimation of equivalent dose in
294 thermoluminescence dating - the *Australian slide* method. *Ancient TL* 11, 1–5.
- 295 R Core Team, 2018. R: A Language and Environment for Statistical Computing. R Foundation
296 for Statistical Computing, Vienna, Austria. <https://r-project.org>.
- 297 Qin, J., Chen, J., Li, Y., Zhou, L., 2018. Initial sensitivity change of K-feldspar pIRIR signals
298 due to uncompensated decrease in electron trapping probability: Evidence from
299 radiofluorescence measurements. *Radiation Measurements* 120, 131–136.
300 doi:10.1016/j.radmeas.2018.06.017
- 301 Richter, D., Pintaske, R., Dornich, K., Krbetschek, M.R., 2012. A novel beta source design for
302 uniform irradiation in dosimetric applications. *Ancient TL* 30, 57–63.
- 303 Richter, D., Richter, A., Dornich, K., 2013. lexsyg — a new system for luminescence research.
304 *Geochronometria* 40, 220–228. doi: 10.2478/s13386-013-0110-0.
- 305 Rieser, U., Habermann, J., Wagner, G.A., 1999. Luminescence dating: A new high sensitivity
306 TL/OSL emission spectrometer. *Quaternary Science Reviews* 18, 311–315. doi:
307 10.1016/S0277-3791(98)00064-X.
- 308 Rieser, U., Hütt, G., Krbetschek, M.R., Stolz, W., 1997. Feldspar IRSL emission spectra at high
309 and low temperatures. *Radiation Measurements* 27, 273–278. doi: 10.1016/S1350-
310 4487(96)00108-4.

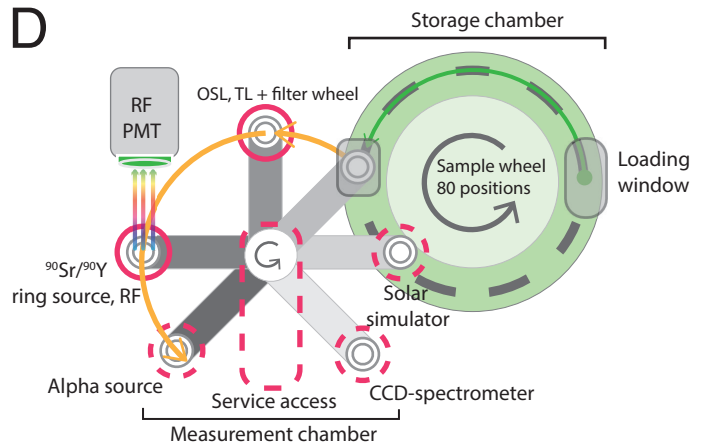
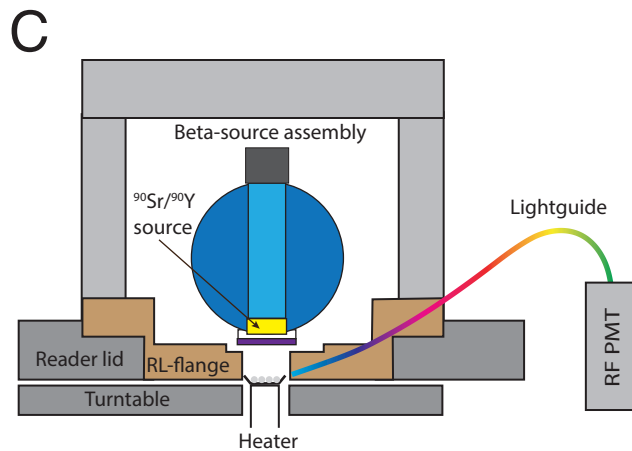
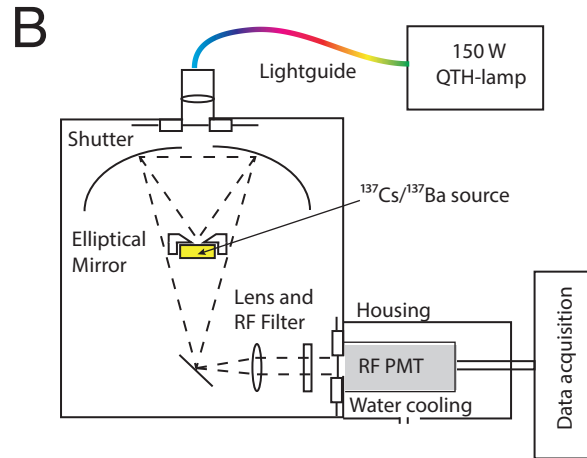
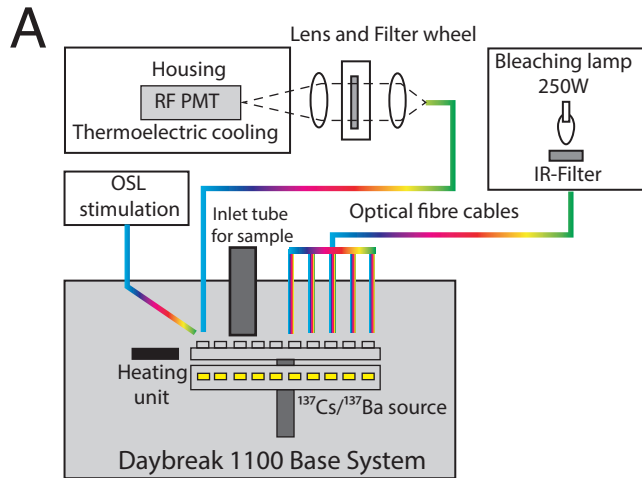
- 311 Rieser, U., Krbetschek, M.R., Stolz, W., 1994. CCD-camera based high sensitivity TL/OSL-
312 spectrometer. *Radiation Measurements* 23, 523–528. doi: 10.1016/1350-4487(94)90092-2.
- 313 Scerri, E.M.L., Shipton, C., Clark-Balzan, L., Frouin, M., Schwenninger, J.-L., Groucutt, H.S.,
314 Breeze, P.S., Parton, A., Blinkhorn, J., Drake, N.A., Jennings, R., Cuthbertson, P., Omari,
315 A.A., Alsharekh, A.M., Petraglia, M.D., 2018. The expansion of later Acheulean hominins
316 into the Arabian Peninsula. *Scientific Reports* 8, 17165. doi: 10.1038/s41598-018-35242-5.
- 317 Schaarschmidt, M., Fu, X., Li, B., Ben Marwick, Khaing, K., Douka, K., Roberts, R.G., 2019.
318 pIRIR and IR-RF dating of archaeological deposits at Badahlin and Gu Myaung Caves –
319 First luminescence ages for Myanmar. *Quaternary Geochronology* 49, 262–270.
320 doi:10.1016/j.quageo.2018.01.001
- 321 Schäfer, J., Laurat, T., Kegler, J. F., 2003. Bericht zu den Ausgrabungen am altsteinzeitlichen
322 Fundplatz Markkleeberg 1999 bis 2001. *Arbeits- und Forschungsberichte zur sächsischen*
323 *Bodendenkmalpfl.* 45, 13–47.
- 324 Schilles, T., 2002. Die Infrarot-Radiolumineszenz von Feldspäten und ihr Einsatz in der
325 Lumineszenzdatierung. PhD thesis, Ruprechts-Karls-Universität Heidelberg, Germany, pp.
326 149.
- 327 Schilles, T., Habermann, J., 2000. Radioluminescence dating: the IR emission of feldspar.
328 *Radiation Measurements* 32, 679–683. doi: 10.1016/S1350-4487(00)00081-0.
- 329 Schmidt, C., Kreutzer, S., DeWitt, R., Fuchs, M., 2015. Radiofluorescence of quartz: A review.
330 *Quaternary Geochronology* 27, 66–77. doi: 10.1016/j.quageo.2015.01.005.
- 331 Schön, M., 1942. Zum Leuchtmechanismus der Kristallphosphore. *Zeitschrift für Physik* 119,
332 463–471. doi: 10.1007/BF01339783.
- 333 Speit, B., Lehmann, G., 1982. Radiation defects in feldspars. *Physics and Chemistry of Minerals*
334 8, 77–82. doi: 10.1007/BF00309017.

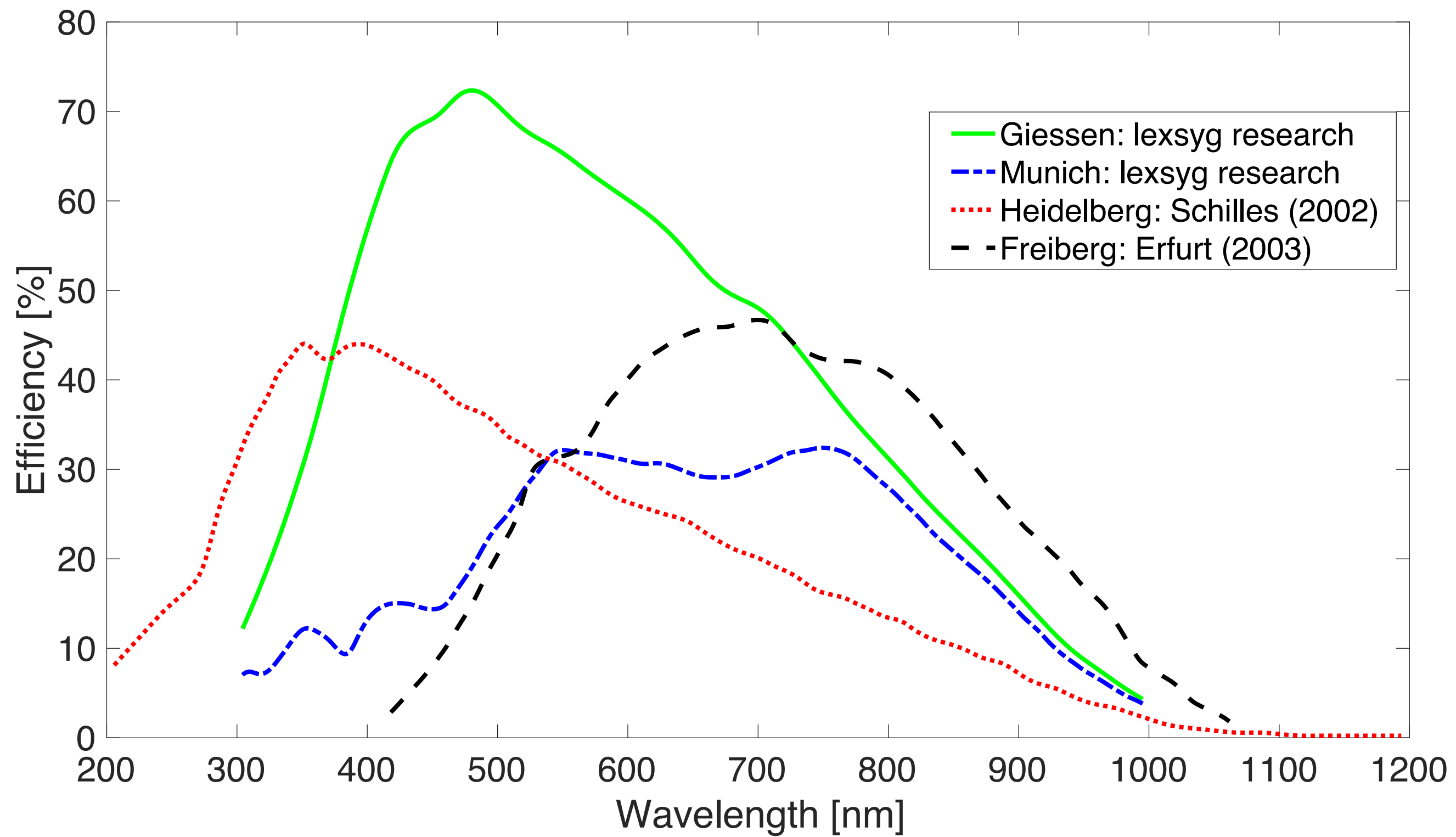
- 335 Spooner, N.A., 1992. Optical dating: Preliminary results on the anomalous fading of
336 luminescence from feldspars. *Quaternary Science Reviews* 11, 139–145.
337 doi:10.1016/0277-3791(92)90055-D
- 338 Sulaymonova, V.A., Fuchs, M.C., Gloaguen, R., Möckel, R., Merchel, S., Rudolph, M.,
339 Krbetschek, M.R., 2018. Feldspar flotation as a quartz-purification method in cosmogenic
340 nuclide dating: A case study of fluvial sediments from the Pamir. *MethodsX* 5, 717–726.
341 doi:10.1016/j.mex.2018.06.014
- 342 Telfer, D.J., Walker, G., 1975. Optical detection of Fe³⁺ in lunar plagioclase. *Nature* 258, 694–
343 695. doi: 10.1038/258694a0.
- 344 Thomsen, K.J., Murray, A.S., Jain, M., Bøtter-Jensen, L., 2008. Laboratory fading rates of
345 various luminescence signals from feldspar-rich sediment extracts. *Radiation Measurements*
346 43, 1474–1486. doi: 10.1016/j.radmeas.2008.06.002.
- 347 Thomsen, K., Murray, A., Jain, M., 2010. Stability of IRSL signals from sedimentary K-feldspar
348 samples. *Geochronometria* 38, 1–13. doi:10.2478/s13386-011-0003-z
- 349 Toyoda, S., Voinchet, P., Falguères, C., Dolo, J.M., Laurent, M., 2000. Bleaching of ESR signals
350 by the sunlight: a laboratory experiment for establishing the ESR dating of sediments.
351 *Applied Radiation and Isotopes* 52, 1357–1362. doi: 10.1016/S0969-8043(00)00095-6.
- 352 Trautmann, T., 1999. Radiolumineszenzuntersuchungen an Feldspat. PhD thesis, Technische
353 Bergakademie Freiberg, Germany, pp. 99.
- 354 Trautmann, T., 2000. A study of radioluminescence kinetics of natural feldspar dosimeters:
355 experiments and simulations. *Journal of Physics D: Applied Physics* 33, 2304–2310. doi:
356 10.1088/0022-3727/33/18/315.
- 357 Trautmann, T., Krbetschek, M.R., Dietrich, A., Stolz, W., 2000a. The basic principle of
358 radioluminescence dating and a localized transition model. *Radiation Measurements* 32,
359 487–492. doi: 10.1016/S1350-4487(00)00119-0.

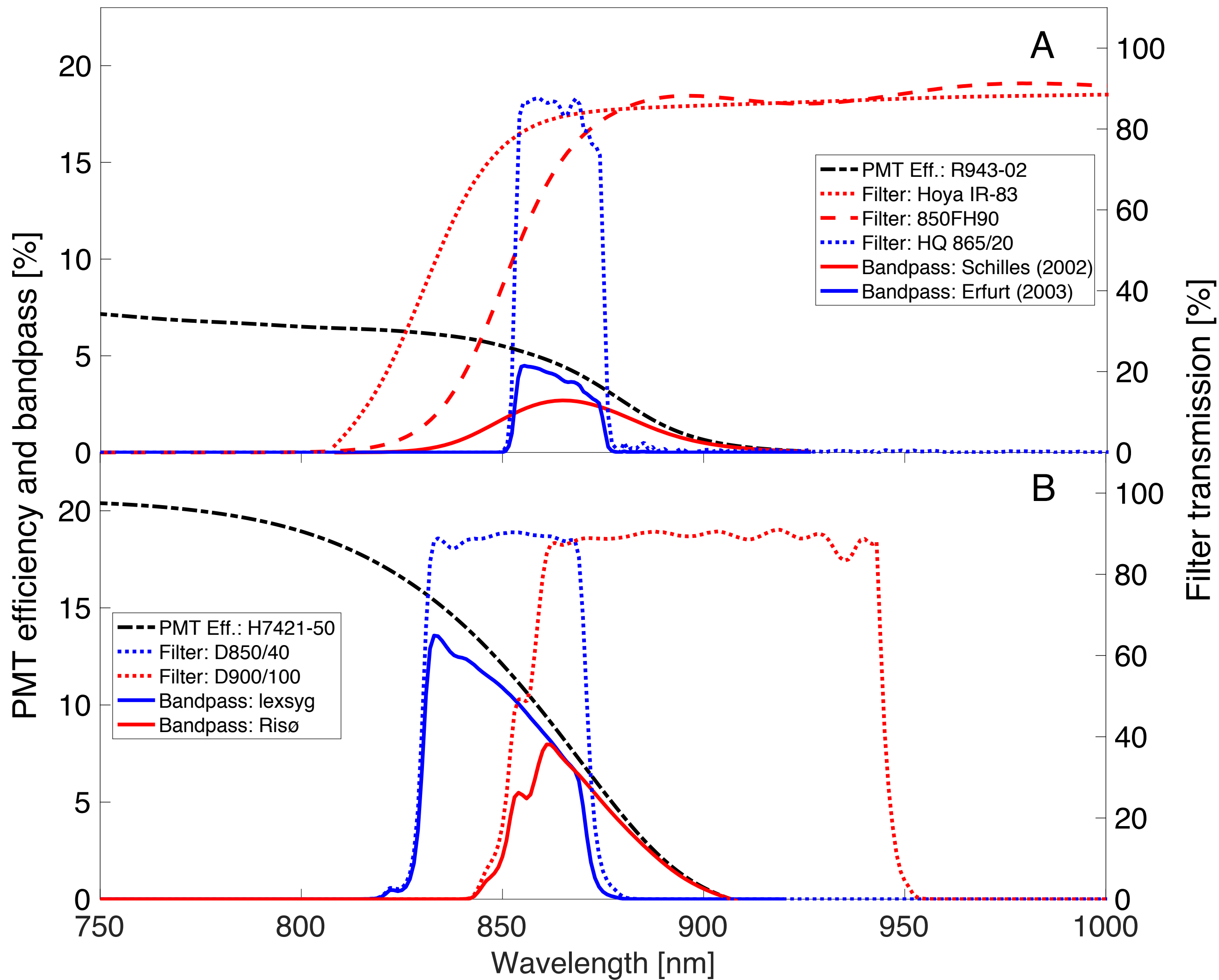
- 360 Trautmann, T., Krbetschek, M.R., Dietrich, A., Stolz, W., 1999a. Feldspar radioluminescence: a
361 new dating method and its physical background. *Journal of Luminescence* 85, 45–58. [https://](https://doi:10.1016/S0022-2313(99)00152-0)
362 [doi:10.1016/S0022-2313\(99\)00152-0](https://doi:10.1016/S0022-2313(99)00152-0).
- 363 Trautmann, T., Dietrich, A., Stolz, W., Krbetschek, M.R., 1999b. Radioluminescence Dating: A
364 New Tool for Quaternary Geology and Archaeology. *Naturwissenschaften* 86, 441–444.
365 doi:10.1007/s001140050649
- 366 Trautmann, T., Krbetschek, M.R., Dietrich, A., Stolz, W., 1998. Investigations of feldspar
367 radioluminescence: potential for a new dating technique. *Radiation Measurements* 29, 421–
368 425. [doi: 10.1016/S1350-4487\(98\)00012-2](https://doi:10.1016/S1350-4487(98)00012-2).
- 369 Trautmann, T., Krbetschek, M.R., Stolz, W., 2000b. A systematic study of the
370 radioluminescence properties of single feldspar grains. *Radiation Measurements* 32, 685–
371 690. [doi: 10.1016/S1350-4487\(00\)00077-9](https://doi:10.1016/S1350-4487(00)00077-9).
- 372 Tsukamoto, S., Jain, M., Murray, A., Thiel, C., Schmidt, E., Wacha, L., Dohrmann, R., Frechen,
373 M., 2012. A comparative study of the luminescence characteristics of polymineral fine
374 grains and coarse-grained K-, and Na-rich feldspars. *Radiation Measurements* 47, 903-908.
375 [https:// doi:10.1016/j.radmeas.2012.02.017](https://doi:10.1016/j.radmeas.2012.02.017).
- 376 Valladas, H., Valladas, G., 1982. Effet de l'irradiation alpha sur des grains de quartz. *PACT* 6,
377 171–178.
- 378 Varma, V., Biswas, R.H., Singhvi, A.K., 2013. Aspects of infrared radioluminescence dosimetry
379 in K-feldspar. *Geochronometria* 40, 266–273. [doi: 10.2478/s13386-013-0125-6](https://doi:10.2478/s13386-013-0125-6).
- 380 Visocekas, R., 1993. Tunneling radiative recombination in K-feldspar sanidine. *Nuclear Tracks*
381 *and Radiation Measurements* 21, 175–178. [doi: 10.1016/1359-0189\(93\)90073-I](https://doi:10.1016/1359-0189(93)90073-I).
- 382 Wagner, G.A., Krbetschek, M.R., Degering, D., Bahain, J.J., Shao, Q., Falguères, C., Voinchet,
383 P., Dolo, J.M., Garcia, T., Rightmire, G.P., 2010. Radiometric dating of the type-site for
384 *Homo heidelbergensis* at Mauer, Germany. *Proceedings of the National Academy of*
385 *Sciences* 107, 19726–19730. [doi: 10.1073/pnas.1012722107](https://doi:10.1073/pnas.1012722107).

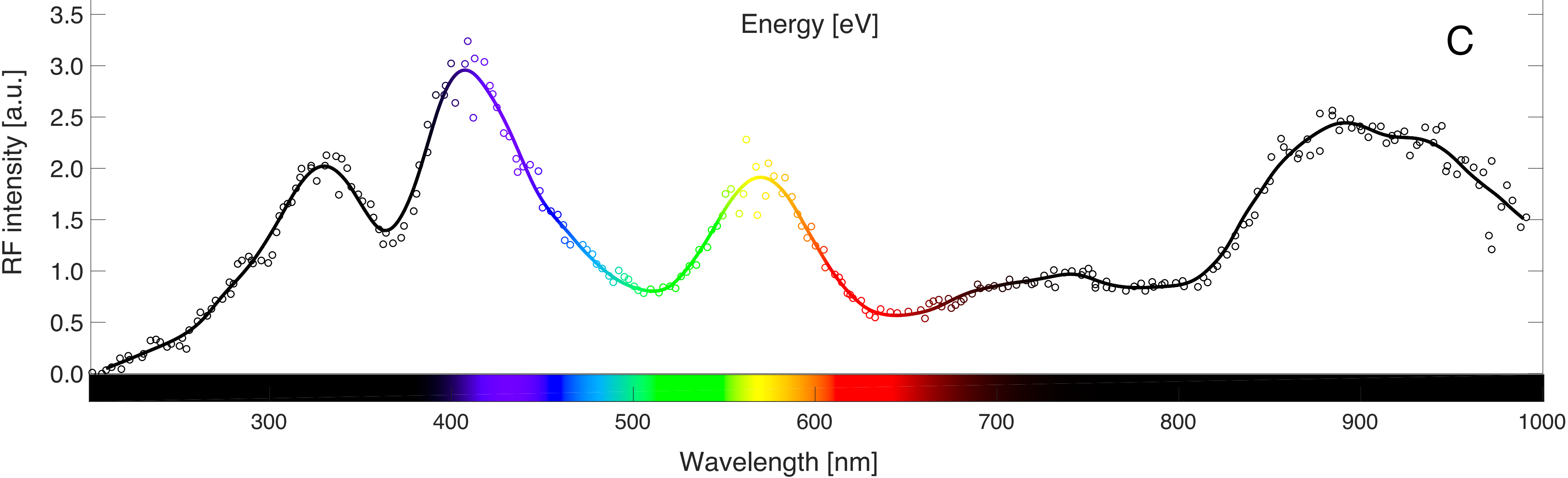
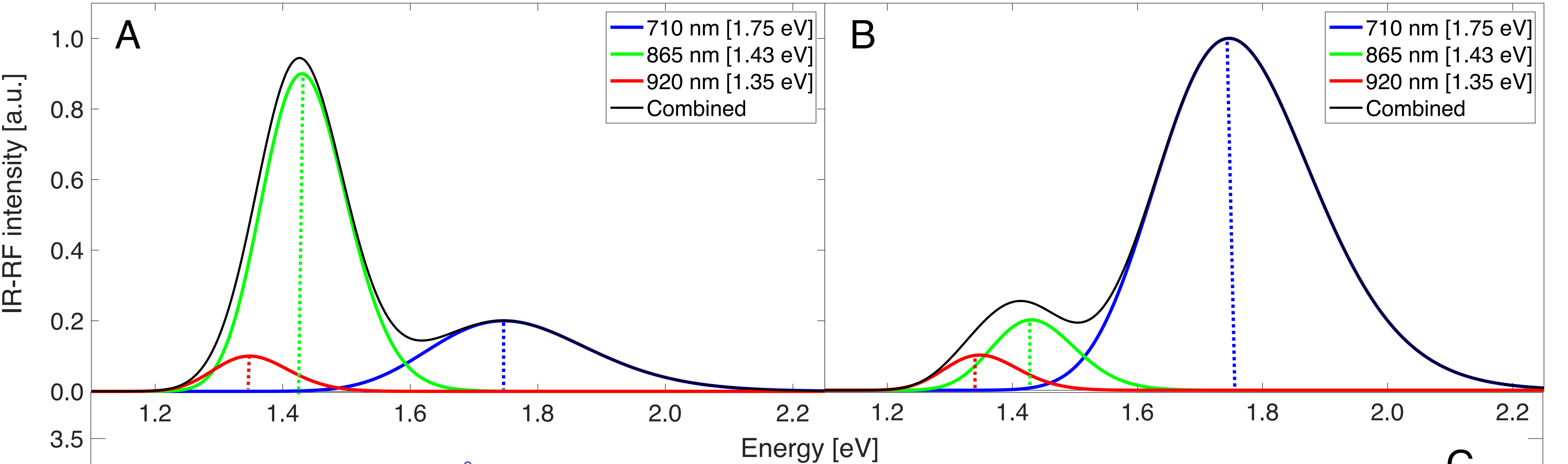
- 386 Wallinga, J., Murray, A., Wintle, A., 2000. The single-aliquot regenerative-dose (SAR) protocol
387 applied to coarse-grain feldspar. *Radiation Measurements* 32, 529-533. doi: 10.1016/S1350-
388 4487(00)00091-3
- 389 White, W.B., Matsumura, M., Linnehan, D.G., Furukawa, T., Chandrasekhar, B.K., 1986.
390 Absorption and luminescence of Fe³⁺ in single-crystal orthoclase. *American Mineralogist* 71,
391 1415–1419.
- 392 Wintle, A.G., 1973. Anomalous fading of thermoluminescence in mineral samples. *Nature* 245,
393 143–144. <https://doi.org/10.1038/245143a0>.
- 394 Wintle, A.G., Murray, A.S., 2006. A review of quartz optically stimulated luminescence
395 characteristics and their relevance in single-aliquot regeneration dating protocols. *Radiation*
396 *Measurements* 41, 369–391. doi: 10.1016/j.radmeas.2005.11.001.
- 397 Wintle, A.G., Adamiec, G., 2017. Optically stimulated luminescence signals from quartz: A
398 review. *Radiation Measurements* 98, 10–33. doi:10.1016/j.radmeas.2017.02.003
- 399 Wünnemann, B., Hartmann, K., Altmann, N., Hambach, U., Pachur, H.-J., Zhang, H., 2007. 22.
400 Interglacial and Glacial Fingerprints from Lake Deposits in the Gobi Desert, NW China. In:
401 Sirocko, F., Claussen, M., Goni, M.F.S., Litt, T. (Eds.), 2007. *The Climate of Past*
402 *Interglacials*. Elsevier., 323–347
- 403 Zhang, J., Li, S.-H., 2020. Review of the Post-IR IRSL Dating Protocols of K-Feldspar. *MPs* 3,
404 7–19. doi:10.3390/mps3010007

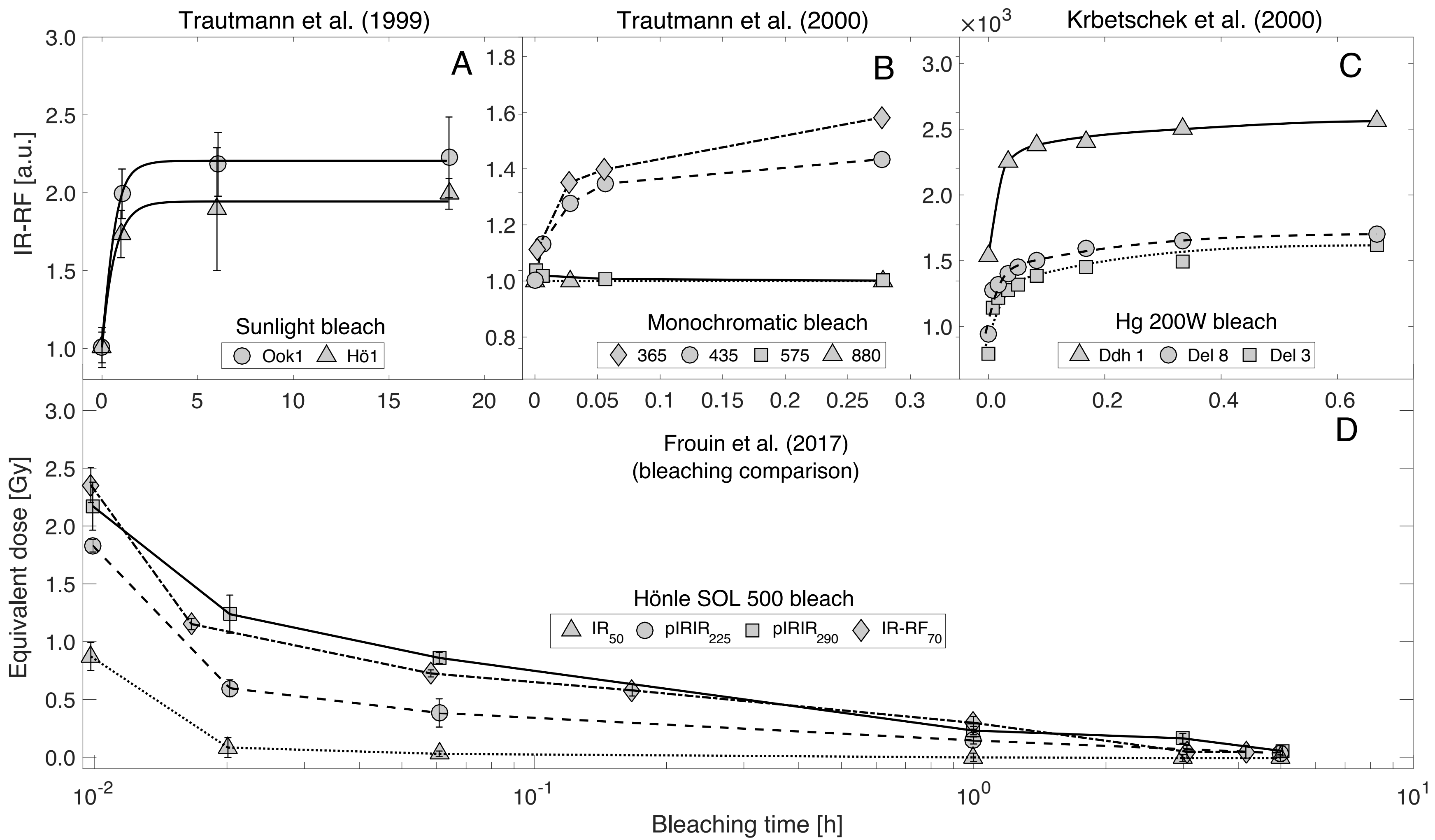


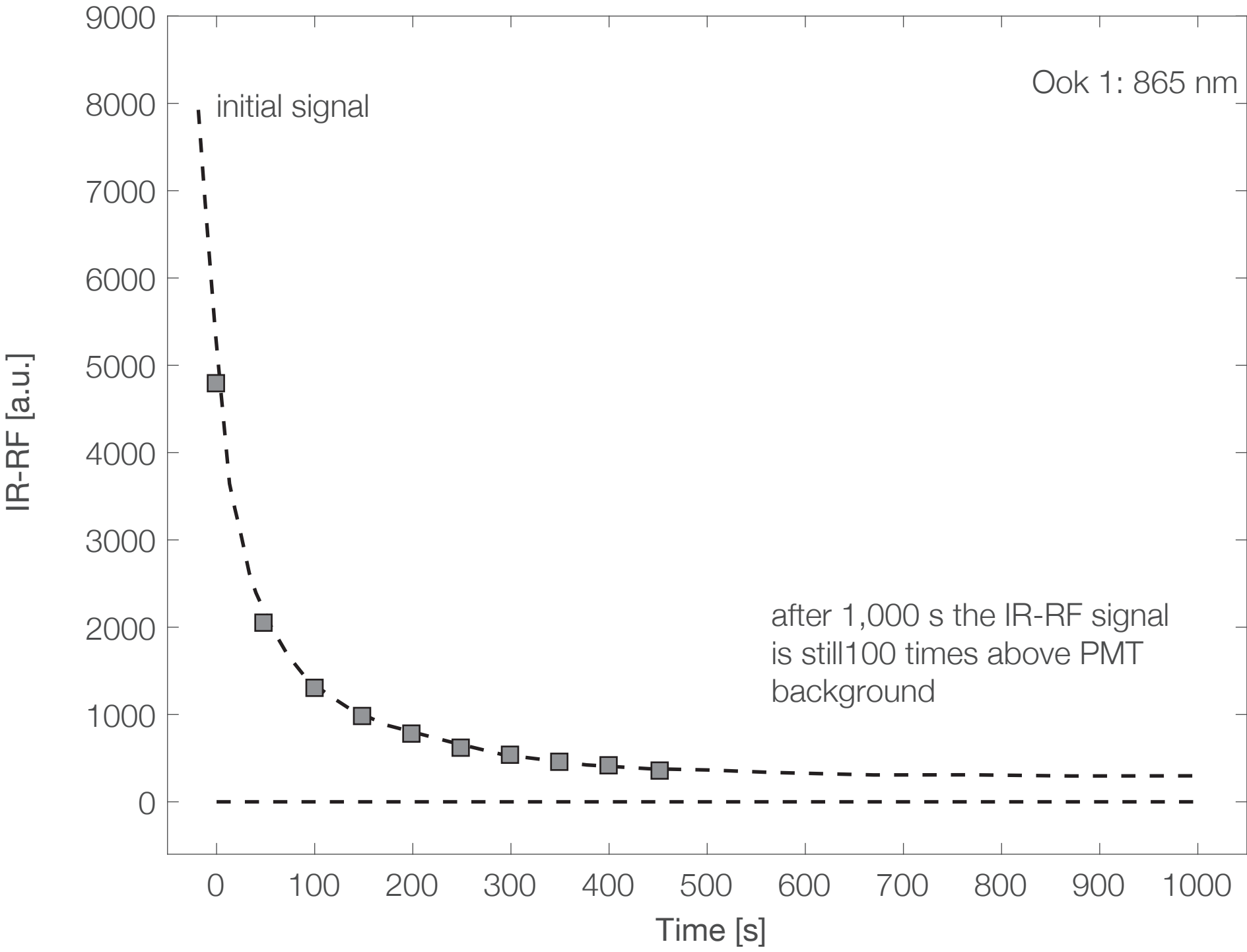










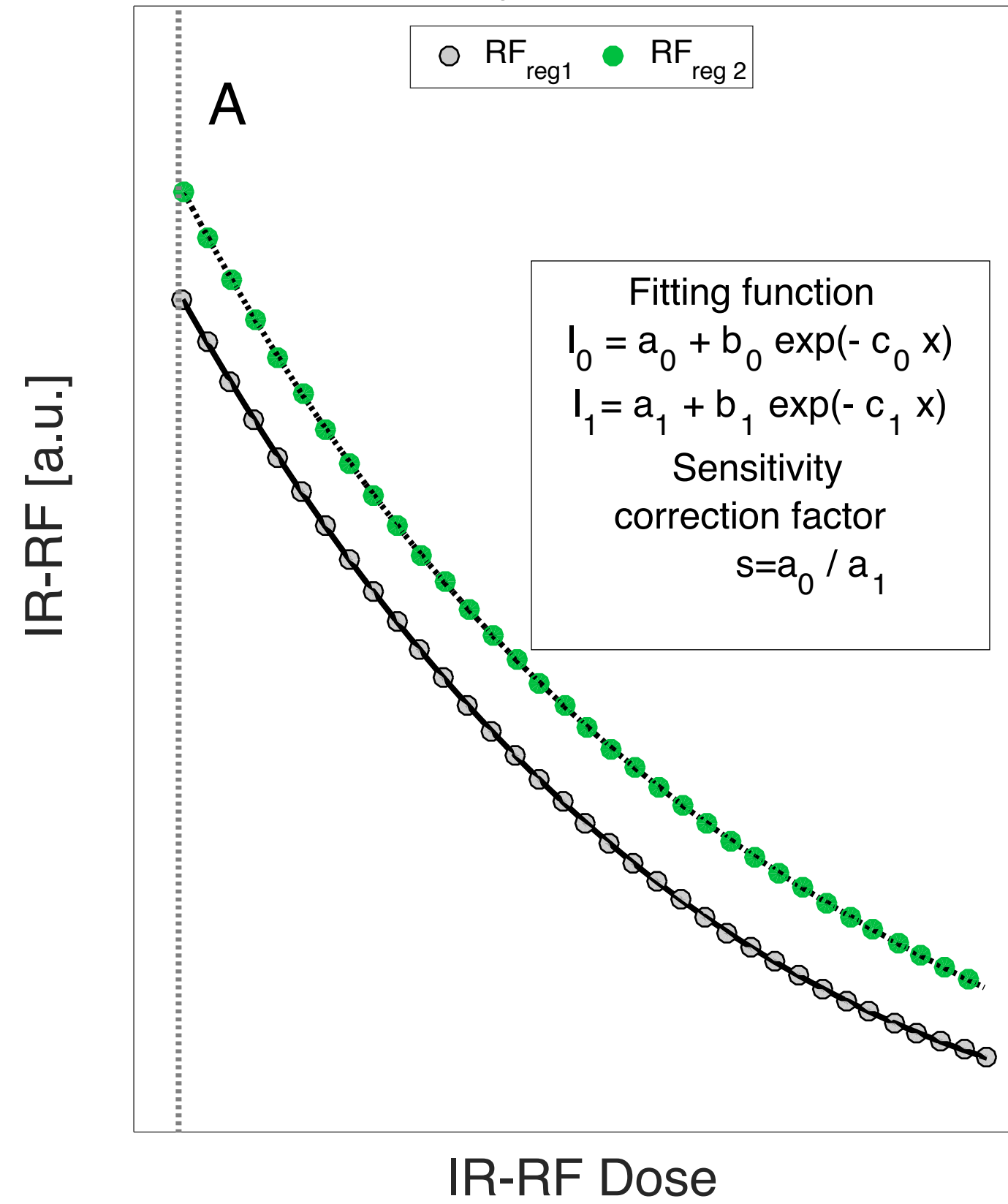


initial signal

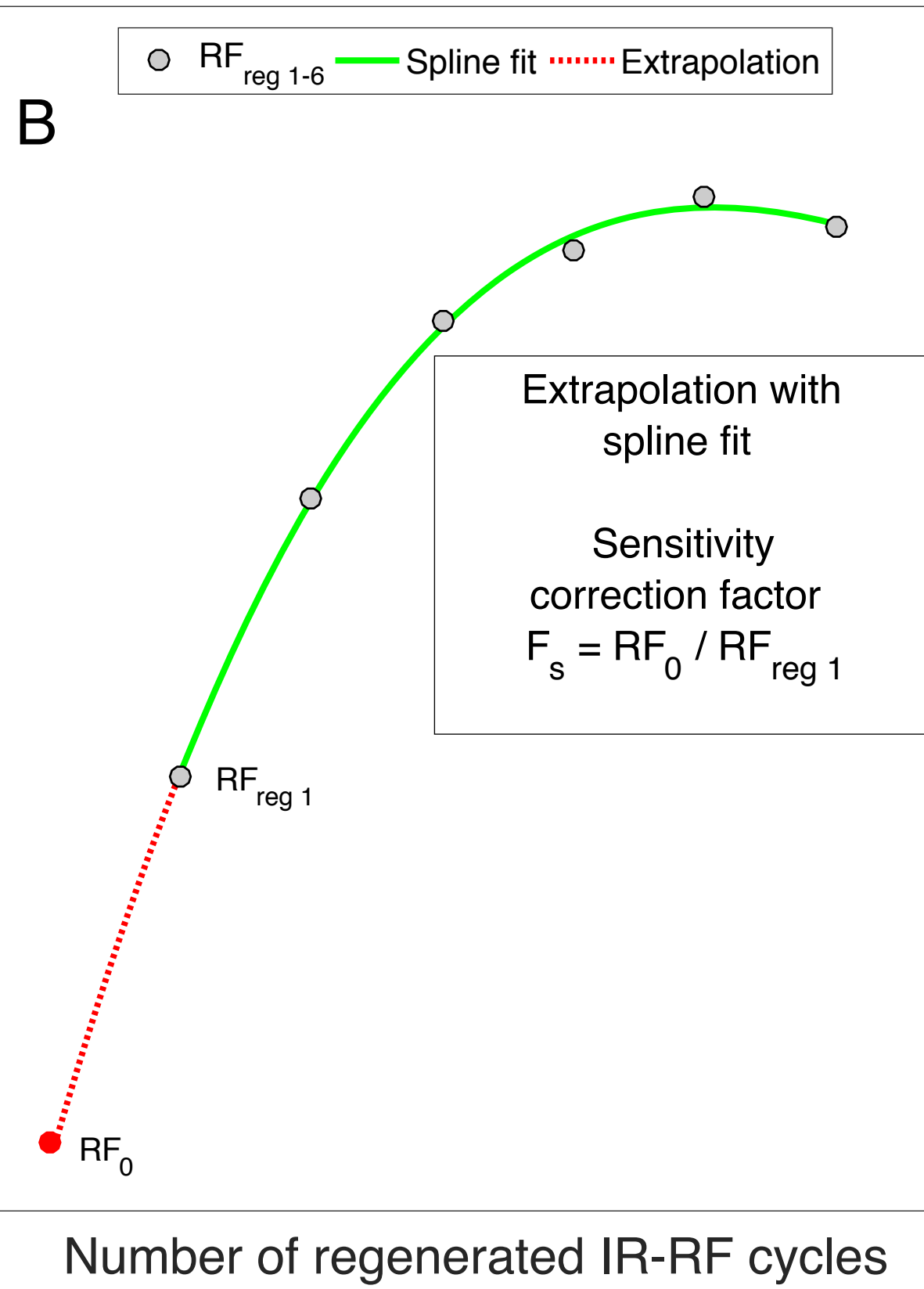
Ook 1: 865 nm

after 1,000 s the IR-RF signal
is still 100 times above PMT
background

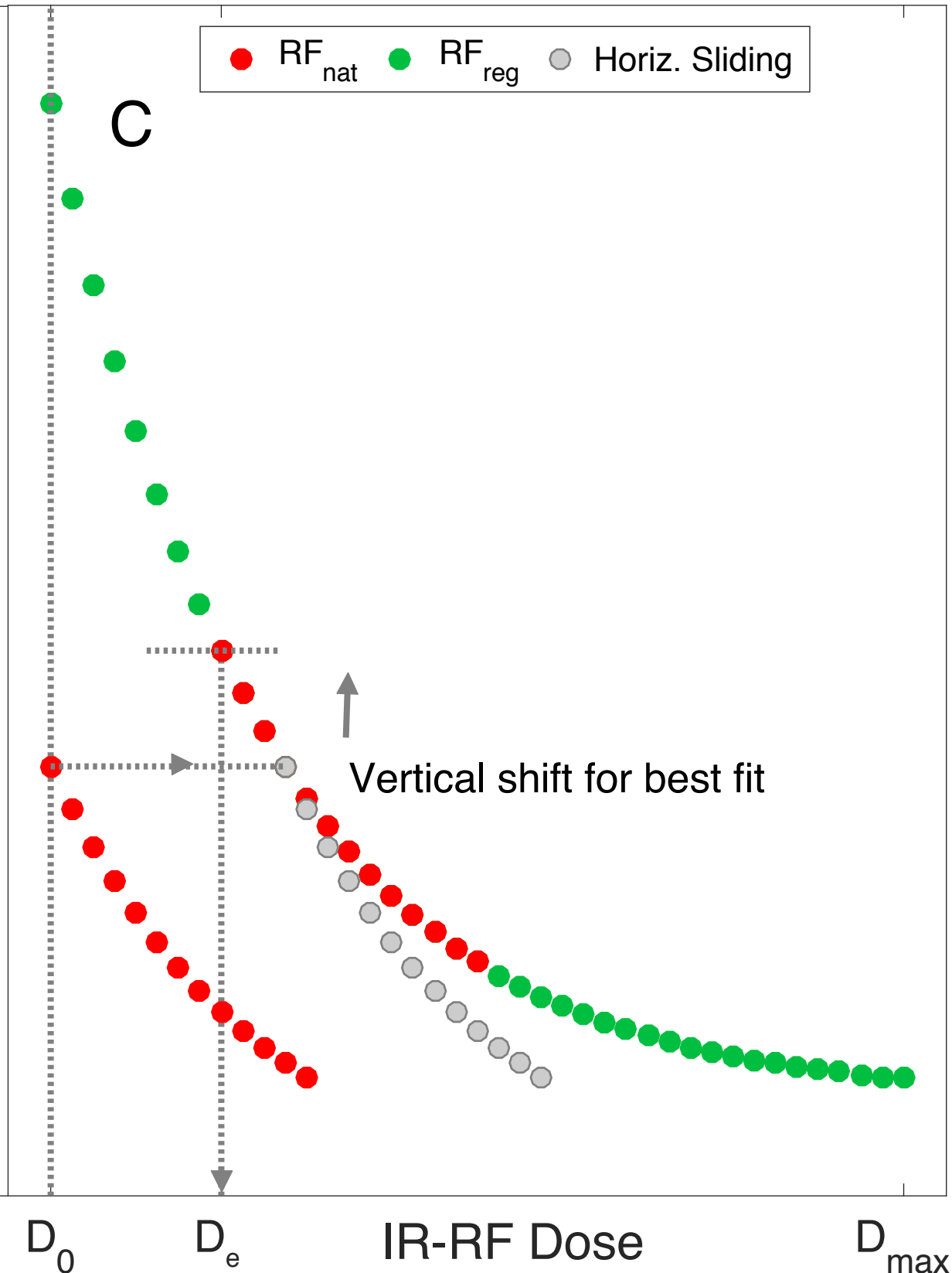
Sensitivity I Schilles (2002)

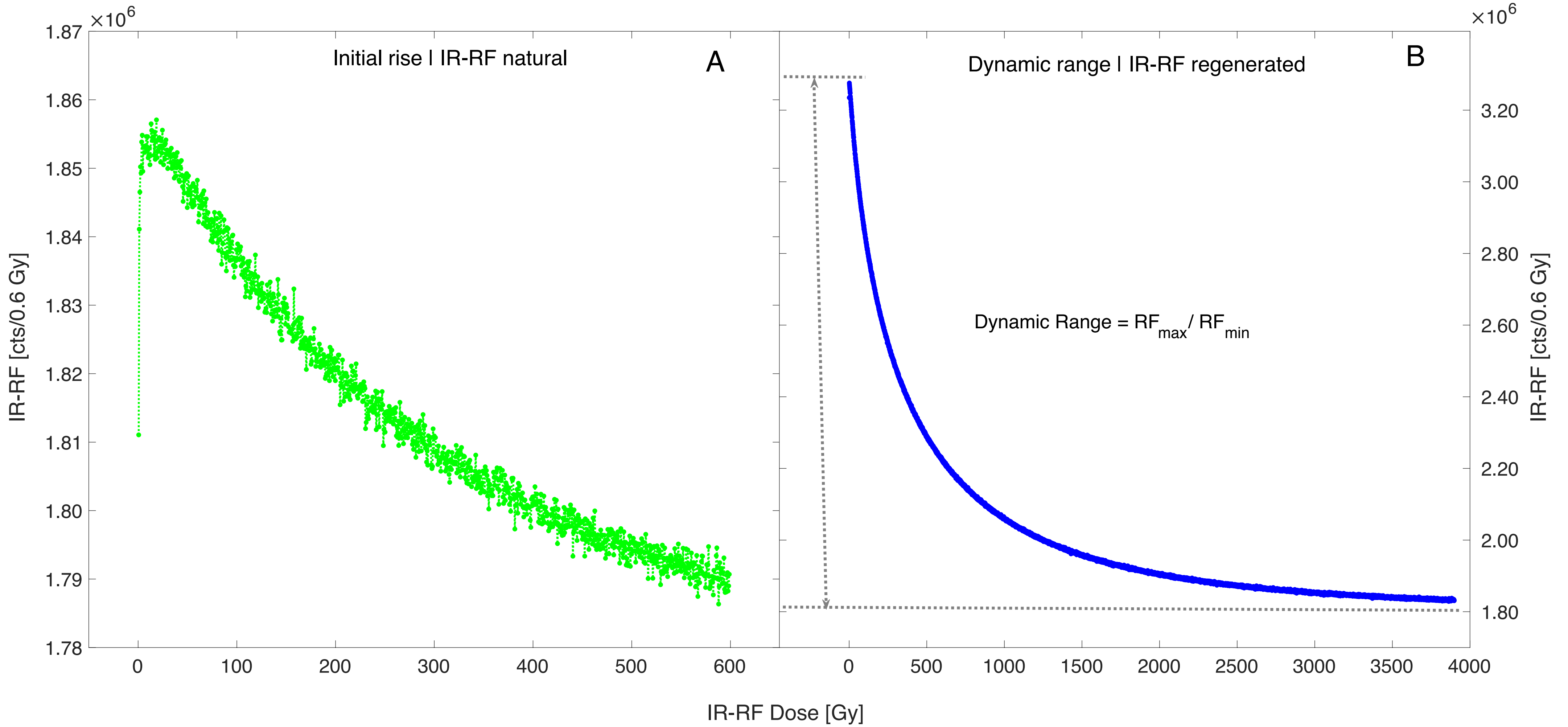


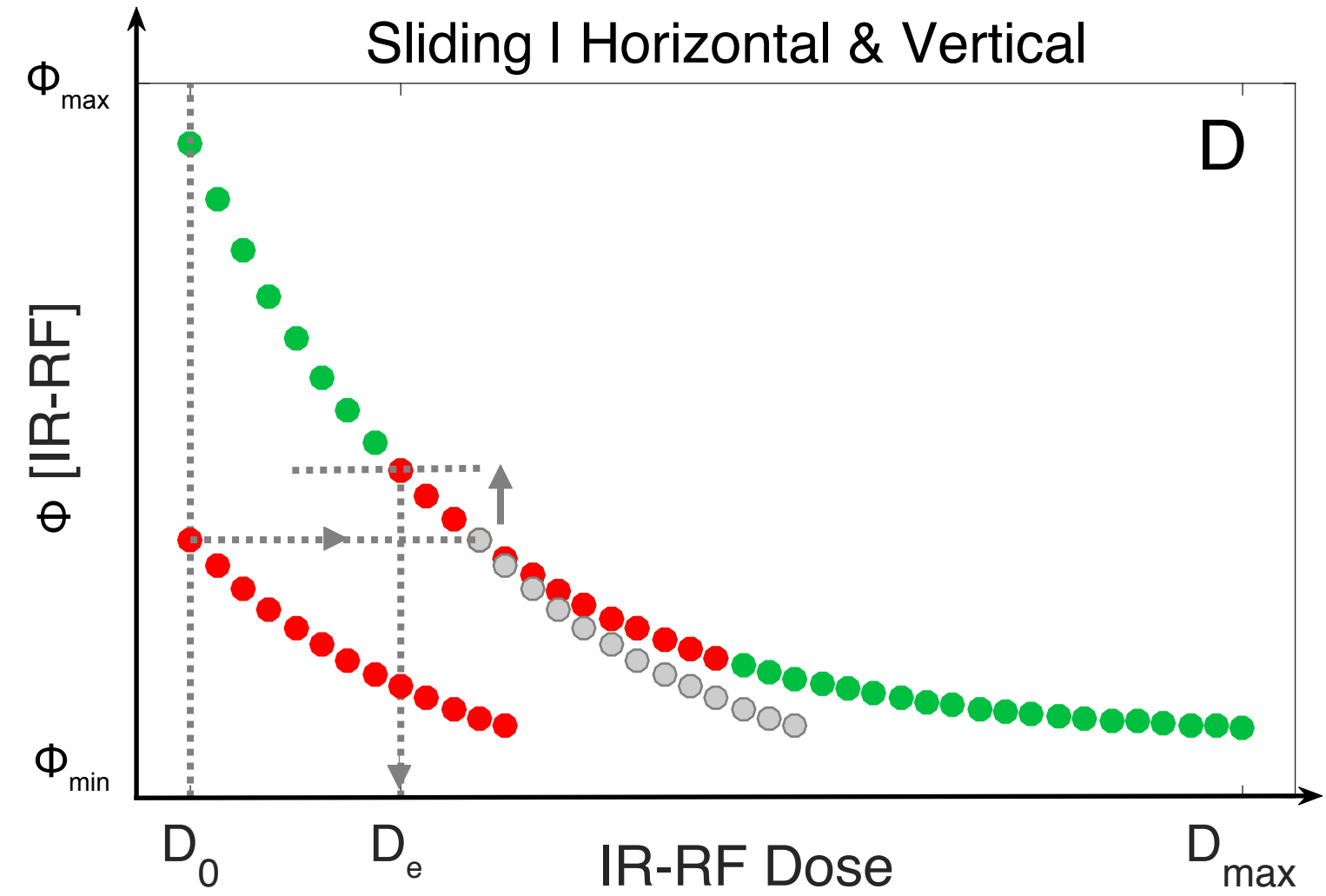
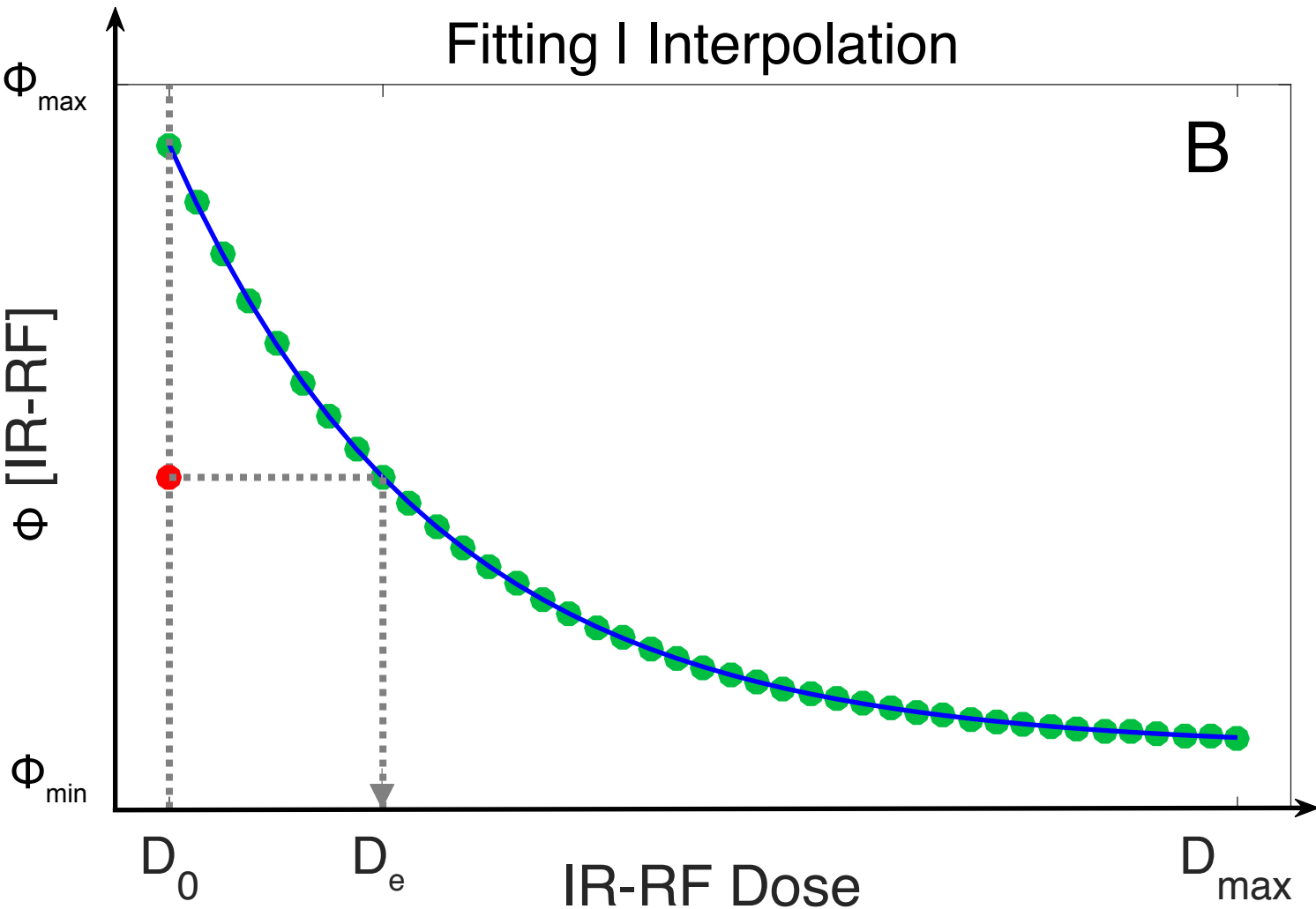
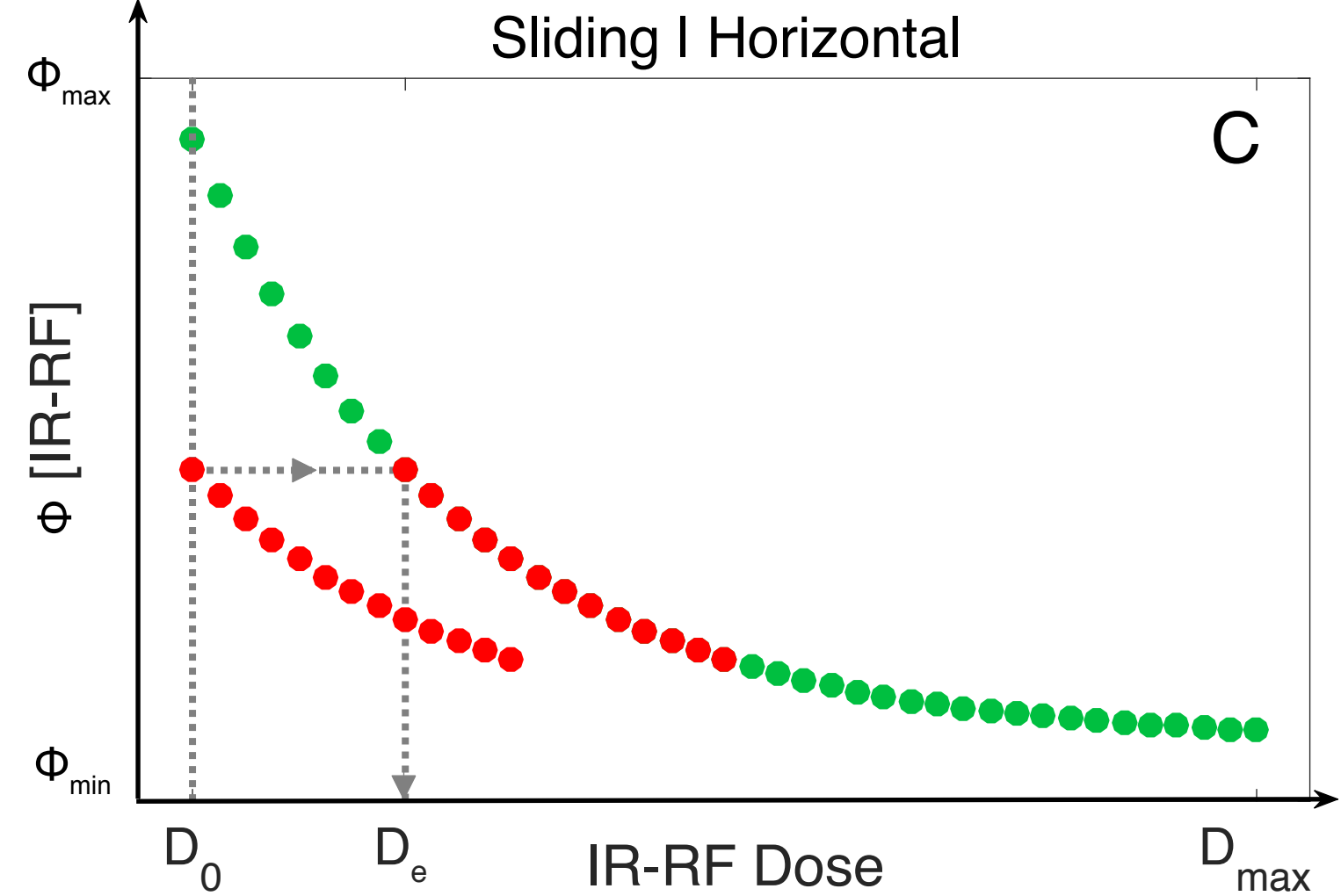
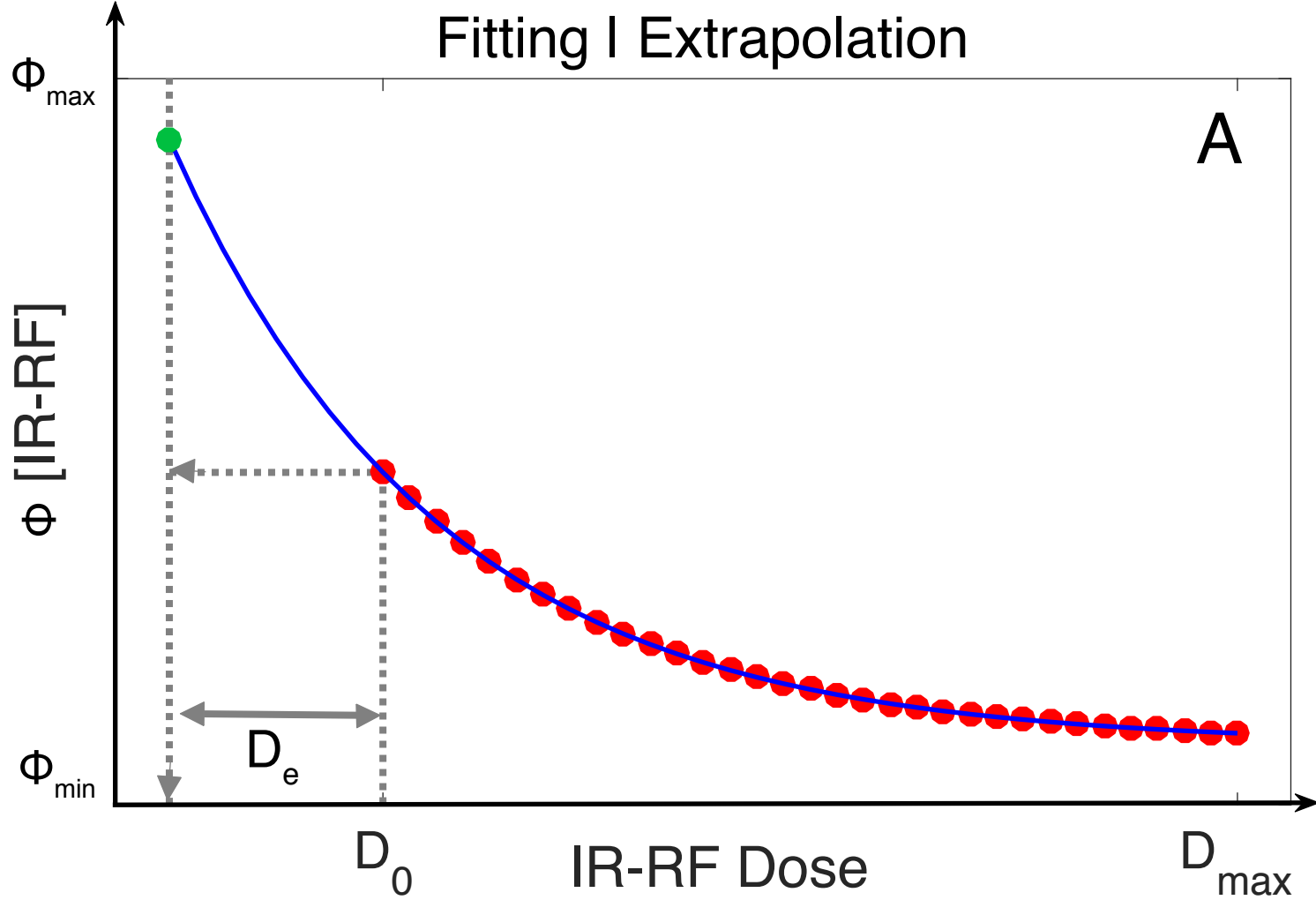
Sensitivity I Varma et al. (2013)



Sensitivity I Murari et al. (2018)







— Fitting ● Natural ● Regenerated ● Horiz. Sliding

Equations used for IR-RF curve fitting

